The Astrophysical Journal, 799:25 (28pp), 2015 January 20 doi:10.1088/0004-637X/799/1/25

AN EMBEDDED ACTIVE NUCLEUS IN THE OH MEGAMASER GALAXY IRAS16399−0937*

Dinalva A. Sales[1,2], A. Robinson[2], D. J. Axon[2,3,8], J. Gallimore[4], P. Kharb[5], R. L. Curran[2], C. O'Dea[2], S. Baum[6], M. Elitzur[7], and R. Mittal[2]
[1] Departamento de Astronomia, Universidade Federal do Rio Grande do Sul. 9500 Bento Gonçalves, Porto Alegre, 91501-970, Brazil
[2] School of Physics and Astronomy, Rochester Institute of Technology, 84 Lomb Memorial Drive, Rochester, NY 14623, USA
[3] School of Mathematical & Physical Sciences, University of Sussex, Falmer, Brighton, BN2 9BH, UK
[4] Department of Physics, Bucknell University, Lewisburg, PA 17837, USA
[5] Indian Institute of Astrophysics, II Block, Koramangala, Bangalore 560034, India
[6] Chester F. Carlson Center for Imaging Science, Rochester Institute of Technology, 54 Lomb Memorial Drive, Rochester, NY 14623, USA
[7] Physics & Astronomy Department, University of Kentucky, Lexington, KY 40506-0055, USA
Received 2014 January 29; accepted 2014 November 1; published 2015 January 13

ABSTRACT

We present a multiwavelength study of the OH megamaser galaxy IRAS16399−0937, based on new *Hubble Space Telescope* (*HST*)/Advanced Camera for Surveys F814W and Hα+[N II] images and archive data from *HST*, Two Micron All Sky Survey, *Spitzer*, *Herschel* and the Very Large Array. This system has a double nucleus, whose northern (IRAS16399N) and southern (IRAS16399S) components have a projected separation of $\sim$6″ (3.4 kpc) and have previously been identified based on optical spectra as a low ionization nuclear emission line region (LINER) and starburst nucleus, respectively. The nuclei are embedded in a tidally distorted common envelope, in which star formation is mostly heavily obscured. The infrared spectrum is dominated by strong polycyclic aromatic hydrocarbon, but deep silicate and molecular absorption features are also present, and are strongest in the IRAS16399N nucleus. The 0.435–500 μm spectral energy distribution was fitted with a model including stellar, interstellar medium and active galactic nucleus (AGN) torus components using our new Markov Chain Monte Carlo code, CLUMPYDREAM. The results indicate that the IRAS16399N contains an AGN ($L_{\rm bol} \sim 10^{44}$ erg s^{-1}) deeply embedded in a quasi-spherical distribution of optically thick clumps with a covering fraction $\approx$1. We suggest that these clumps are the source of the OHM emission in IRAS16399−0937. The high torus covering fraction precludes AGN photoionization as the origin of the LINER spectrum, however, the spectrum is consistent with shocks ($v \sim$ 100–200 km s^{-1}). We infer that the $\sim 10^8\,M_\odot$ black hole in IRAS16399N is accreting at a small fraction ($\sim$1%) of its Eddington rate. The low accretion rate and modest nuclear star formation rates suggest that while the gas-rich major merger forming the IRAS16399−0937 system has triggered widespread star formation, the massive gas inflows expected from merger simulations have not yet fully developed.

Key words: galaxies: active – galaxies: individual (IRAS16399–0937, IRASF16399–0937) – galaxies: interactions – galaxies: irregular – galaxies: ISM – galaxies: starburst – infrared: galaxies – radio continuum: galaxies

1. INTRODUCTION

Luminous infrared galaxies (LIRGs) dominate the bright end of the galaxy luminosity function in the nearby universe ($z \lesssim$ 0.3; Soifer et al. 1987) and are known to host both starbursts and active galactic nuclei (AGNs), frequently in the same system. A variety of observational evidence—such as double nuclei, starburst activity, and disturbed morphologies—suggests that most LIRGs ($L \gtrsim 10^{11}\,L_\odot$) are gas-rich disk galaxies that are undergoing strong interactions or mergers. The most luminous systems, ultra-luminous infrared galaxies (ULIRGs), have quasar-like luminosities ($L \gtrsim 10^{12}\,L_\odot$) and all appear to be advanced mergers (see Sanders & Mirabel 1996 for a review). Much observational and theoretical work has established that mergers of gas-rich galaxies play a key role in galaxy evolution (e.g., Sanders et al. 1988a; Barnes & Hernquist 1992; Hopkins et al. 2006; Haan et al. 2011): tidal torques generated by the merger drive gas into the galaxy core(s), triggering starbursts and fueling embedded AGNs. It has been proposed that in this scenario, "cool" starburst-dominated (U)LIRGs evolve into "warm" AGN-dominated ULIRGs as the circumnuclear dust is dispersed by starburst and AGN-induced outflows (Sanders et al. 1988b).

However, the role of galaxy mergers in triggering AGNs remains uncertain. There is increasing evidence that major mergers only trigger the most luminous AGNs, while less luminous AGNs seem to be driven by secular processes (e.g., Treister et al. 2012). Furthermore, in their study of 62 ULIRGs, Rigopoulou et al. (1999) found no correlation between merger stage and evidence of AGN activity, suggesting that an AGN-dominated system is not an inevitable outcome of a gas-rich merger and that ULIRG evolution is strongly affected by the available gas mass and the individual structures of the progenitor galaxies.

Approximately 20% of (U)LIRGs contain extremely luminous OH masers, emitting primarily in the 1667 and 1665 MHz lines with luminosities $\sim 10^{2-4}\,L_\odot$ (Darling & Giovanelli 2002; Lo 2005). In the most recent and well-developed models, this OH megamaser (OHM) emission is produced by amplification of a background radio continuum source by clumps of molecular gas, with inverted level populations arising from pumping by far infra-red (FIR; $\sim$50 μm) radiation from dust heated by a starburst and/or an embedded AGN (e.g., Baan 1985;

* Based partly on observations made with the NASA/ESA *Hubble Space Telescope*, obtained (from the data archive) at the Space Telescope Science Institute, which is operated by the Association of Universities for Research in Astronomy, Inc., under NASA contract NAS 5-26555.
[8] 1951–2012.

Parra et al. 2005; Lockett & Elitzur 2008). As they are found in gas-rich mergers, it has been suggested that OHMs can be used to trace galaxy merger rates and associated processes (dust obscured star formation and black hole growth) over a wide redshift range (e.g., Lo 2005, and references therein). Moreover, studies of local OH megamaser galaxies (OHMGs) seem likely to provide important insights into processes occurring in gas-rich mergers. Thus, it has been argued that OHM emission requires exceptionally high concentrations of dense molecular gas, perhaps associated with a temporal spike in tidally driven gas inflow (Darling 2007). In some individual OHMGs, detailed interferometric mapping studies have found that the OH masers arise in dense, edge-on rotating molecular gas disks or rings on scales $\leqslant$100 pc, which have been identified as compact starburst rings in some objects (Rovilos et al. 2002; Parra et al. 2005; Momjian et al. 2006), or in others as the circumnuclear torii (Yates et al. 2000; Klöckner & Baan 2004; Pihlström et al. 2005; Richards et al. 2005) hypothesized by the unified scheme for AGNs (Antonucci & Miller 1985; Antonucci 1993; Urry & Padovani 1995). In addition, the OH lines often show broad asymmetric profiles and velocity shifts suggestive of outflows, particularly in systems containing optically identified AGNs (Darling & Giovanelli 2006), perhaps indicating that starburst- or AGN-driven outflows are clearing away enshrouding dense molecular material.

In this paper we present a detailed multiwavelength study of IRAS16399−0937, a spectacular but relatively little studied interacting galaxy pair at a redshift $z = 0.027$. It is both an LIRG ($L_{\rm FIR} \approx 10^{11.2}\ L_{\odot}$) and an OHMG ($L_{\rm OH} \approx 10^{1.7}\ L_{\odot}$). The OHM emission has a flux $\sim 1.3 \times 10^{-22}$ W m^{-2}, with a peak flux density at 1.6 GHz of $\sim$25 mJy (Staveley-Smith et al. 1986, 1992; Norris et al. 1989). Morphologically, IRAS16399−0937 is a mid-to-late stage merger, with a double nucleus situated in a common envelope (Haan et al. 2011). Baan et al. (1998) classified the northern nucleus (denoted IRAS16399N hereafter) as a low ionization nuclear emission line region (LINER; see Heckman 1980) and the southern nucleus (denoted IRAS16399S hereafter) as a starburst, based on the optical emission line ratios (Baldwin et al. 1981; Veilleux & Osterbrock 1987). Therefore, IRAS16399−0937 appears to contain both an AGN and a starburst in a merging system, making it a good system in which to study the relative importance of star formation and black hole accretion in powering the IR emission.

Our study is based on new *Hubble Space Telescope* (*HST*) imaging observations and an analysis of archival *Spitzer*, *Herschel*, and Very Large Array (VLA) data. The paper is organized as follows. In Sections 2 and 3 we describe the data reduction procedures and the measurements and results obtained, including inferred star formation rates (SFRs). In Section 4 we present a decomposition of the optical–IR spectral energy distribution (SED), using a new, robust fitting technique. We discuss the implications of our results in Section 5. The main results and conclusions are summarized in Section 6. Throughout this paper, we adopt the Hubble constant as $H_0 = 67.3 \pm 1.2$ km s^{-1} Mpc^{-1}, $\Omega_{\Lambda} = 0.73$, and $\Omega_m = 0.27$ (Planck Collaboration et al. 2013; Lahav & Liddle 2014).

2. OBSERVATION AND DATA REDUCTION

2.1. Hubble Space Telescope Images

We observed IRAS16399−0937 using the *HST* Advanced Camera for Surveys (ACS) as part of a snapshot program to obtain continuum and emission line imaging of a large sample of OHMGs (Program id 11604; PI: D. J. Axon). Images of IRAS16399−0937 were acquired in the wide-field channel (WFC) using the broad-band F814W filter and the narrow and medium band ramp filters, FR656N and FR914M, respectively. The broad-band image in F814W was obtained to map the continuum morphology of the host galaxy. The ramp filter images were obtained to study the ionized gas distribution, with the central wavelengths set to cover Hα in the narrow-band filter and the nearby continuum, for continuum subtraction, in the medium-band filter. The band pass of the FR656N ramp filter includes Hα and the [N II] λ6548, 83 lines. The total integration times were 600 s in the broad-band (*I*) F814W filter, 200 s in the medium-band FR914M filter, and 600 s in the narrow band Hα FR656N filter.

In addition to the new ACS images, we also retrieved B and H broad-band images of IRAS16399−0937 from the Hubble Legacy Archive.[9] These images were obtained with the ACS/WFC and NICMOS2 cameras using the F435W and F160W filters as part of Programs 10592 (PI: Aaron Evans) and 11235 (PI: Jason Surace), respectively. Both images were enhanced data products generated from the standard *HST* pipeline.

The pipeline image products were used for further processing with IRAF[10] packages. Cosmic rays were removed from individual images using the IRAF task *lacos$_{im}$* (van Dokkum 2001). Finally, the standard IRAF tasks were used to yield one final reduced image for each filter (see Figure 1).

In order to construct a continuum free Hα+[N II] image of IRAS16399−0937, we first measured count rates for several foreground stars in both the medium-band (FR914M) and narrow-band (FR656N) ramp filter images. A mean scaling factor was determined from the count rate ratios and applied to the medium-band FR914M image, which was then subtracted from the narrow-band FR656N image. Finally, the continuum subtracted image Hα+[N II] was visually inspected to confirm that the residuals at the positions of the foreground stars are negligible. This is a well established procedure that turns out in practice to give typical uncertainties of 5%–10% (see Hoopes et al. 1999; Rossa & Dettmar 2000, 2003)

2.2. Spitzer Mid-infrared Data

Infrared spectroscopy and image data of IRAS16399−0937 were extracted from the *Spitzer Space Telescope* archive. The IRAC and MIPS images were obtained in *Spitzer* program 3672 (PI: J. Mazzarella). *Spitzer*'s IRAC camera is composed of four channels covering a area of 5.′2×5.′2 at 3.6, 4.5, 5.8, and 8.0 μm. All four detectors have a 256×256 array of pixels, with each pixel having a size of 1.″2×1.″2. The FWHM of the IRAC point response function varies between 1.″7 and 2.″0 from channels 1 (3.6 μm) to 4 (8.0 μm), so the two nuclei of IRAS16399−0937 are well resolved in all the IRAC bands.

The *Spitzer* MIPS instrument employs three detector arrays that provide imaging and photometry at 24, 70, and 160 μm, respectively. The 24 μm, 70 μm, and 160 μm arrays have pixel sizes of 2.″5, 5.″2 (in narrow field of view mode), and 16″×18″pixel^{-1}, respectively. As the point-spread function at

[9] Based on observations made with the NASA/ESA *Hubble Space Telescope*, and obtained from the Hubble Legacy Archive, which is a collaboration between the Space Telescope Science Institute (STScI/NASA), the Space Telescope European Coordinating Facility (ST-ECF/ESA) and the Canadian Astronomy Data Centre (CADC/NRC/CSA).

[10] IRAF is distributed by the National Optical Astronomy Observatory, which is operated by the Association of Universities for Research in Astronomy (AURA), Inc., under cooperative agreement with the National Science Foundation.

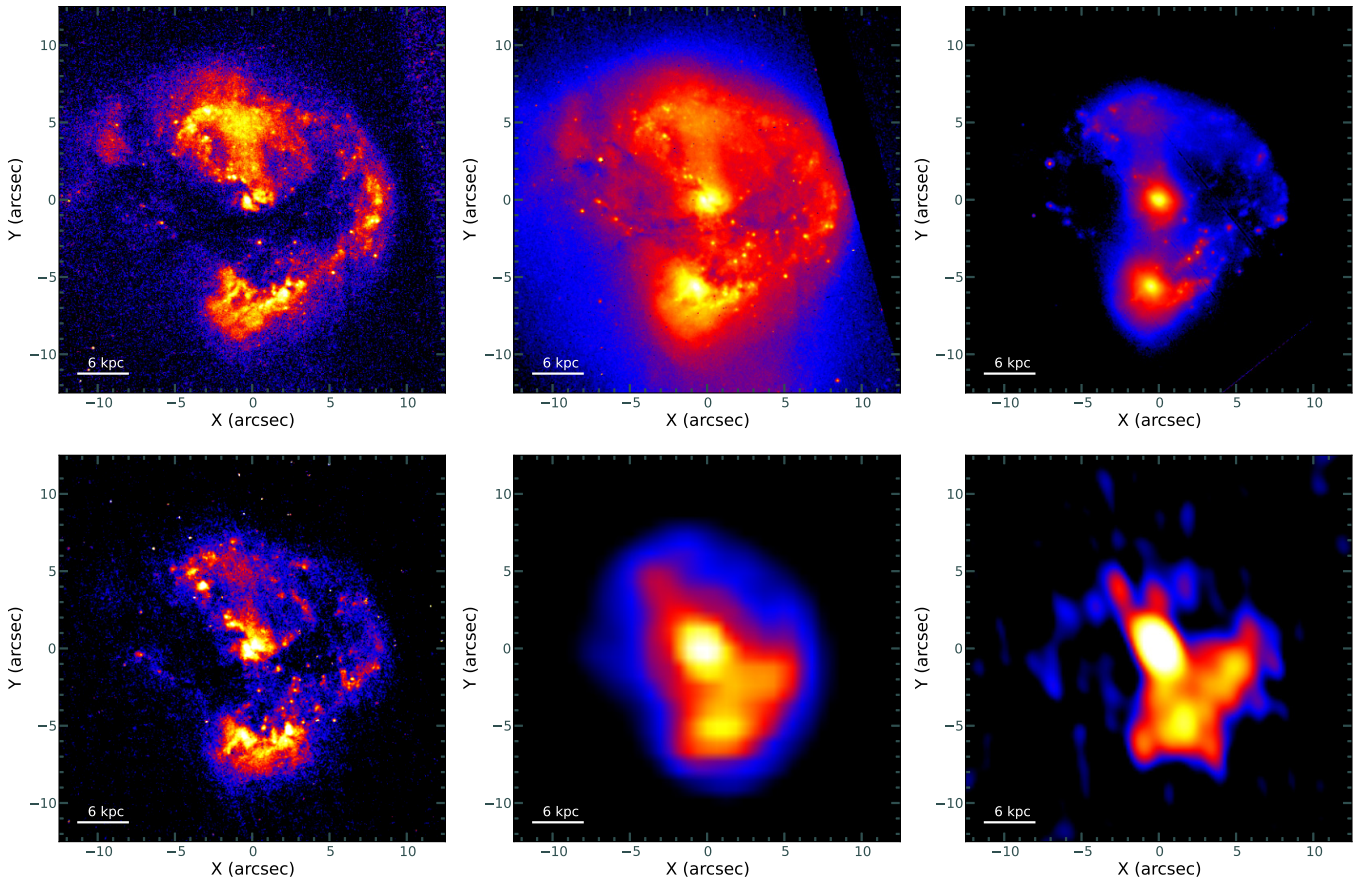

Figure 1. Multiwavelength images of IRAS16399−0937. Top panels, from the left to the right: *HST* images obtained with ACS F435W (left), ACS F814W (middle), NICMOS F160W (1.6 μm, right). Bottom panels: continuum-subtracted Hα+[N II], from *HST* ACS (left), ISM PAH-dust 8.0 μm emission, from *Spitzer* IRAC (middle), VLA 1.49 GHz (right). North is up and east is to the left.

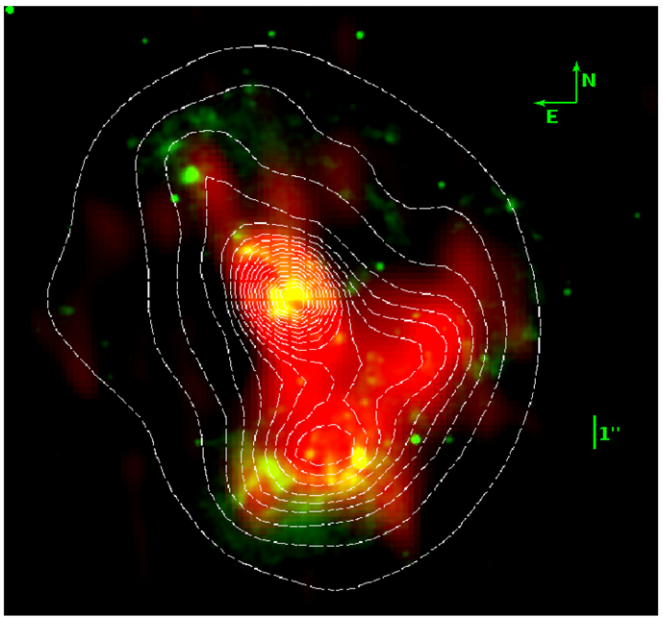

Figure 2. Composite image of IRAS16399−0937. The green and red channels represent the Hα+[N II] and 1.49 GHz VLA images, respectively. The contours (dotted lines) show the ISM PAH-dust 8 μm emission (contours are linear and stepped in 10% increments of the peak).

these wavelengths has FWHMs of 6″, 18″, and 40″, respectively, the two nuclei are not spatially resolved in the MIPS images.

To avoid saturation of the bright source, IRAS16399−0937 was imaged with IRAC at 3.6, 4.5, 5.8, and 8.0 μm and MIPS at 24, 70, and 160 μm using short integration times (see Armus et al. 2009; Petric et al. 2011). For the data reduction and mosaicking of IRAC and MIPS images, we use corrected BCD and filtered BCD image data from versions 18.18 and 18.12 of the pipeline, respectively. These data were used as input to the software package MOPEX[11] (Makovoz & Khan 2005; Makovoz et al. 2005). In order to extract and estimate the galaxy photometric fluxes in each IRAC and MPIS filter, we used the APEX package of the MOPEX code (Makovoz & Marleau 2005). The flux error for each passband includes the combined effect of uncertainty caused by post processing of the images, as well as that of the flux density calibration of the instruments (Fazio et al. 2004; Rieke et al. 2004). Hence, we computed the flux uncertainty by measuring the residual flux density from the background subtracted images (typically ∼2%; Reach et al. 2005) and adding an absolute flux calibration uncertainty of 10% for the IRAC and MIPS 24 μm measurements, and of 20% for MIPS 70 and 160 μm fluxes.[12] Our measured flux densities and uncertainties are given in Table 1. A composite image of IRAS16399−0937 using Hα, 1.49 GHz, and 8.0 μm is presented in Figure 2.

[11] http://irsa.ipac.caltech.edu/data/SPITZER/docs/dataanalysistools/
[12] http://irsa.ipac.caltech.edu/data/SPITZER/docs/

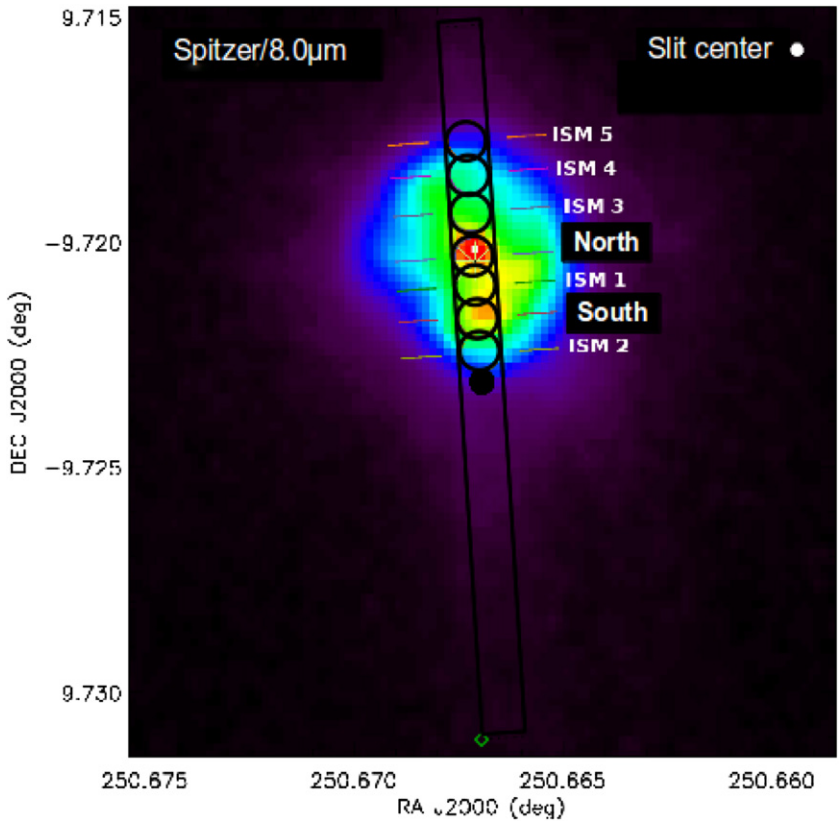

Figure 3. *Spitzer* IRAC 8 μm image showing the apertures used within SMART to extract IRS SL module spectra. The slit position is indicated by solid parallel lines. The SMART apertures are circular, each having a radius of 2.″02. Two apertures are centered on the IRAS16399N (LINER) and IRAS16399S (SB) nuclei, respectively, the other five (ISM 1, 2, 3, 4, and 5) sample the extended envelope. The corresponding spectra are shown in Figure 5.

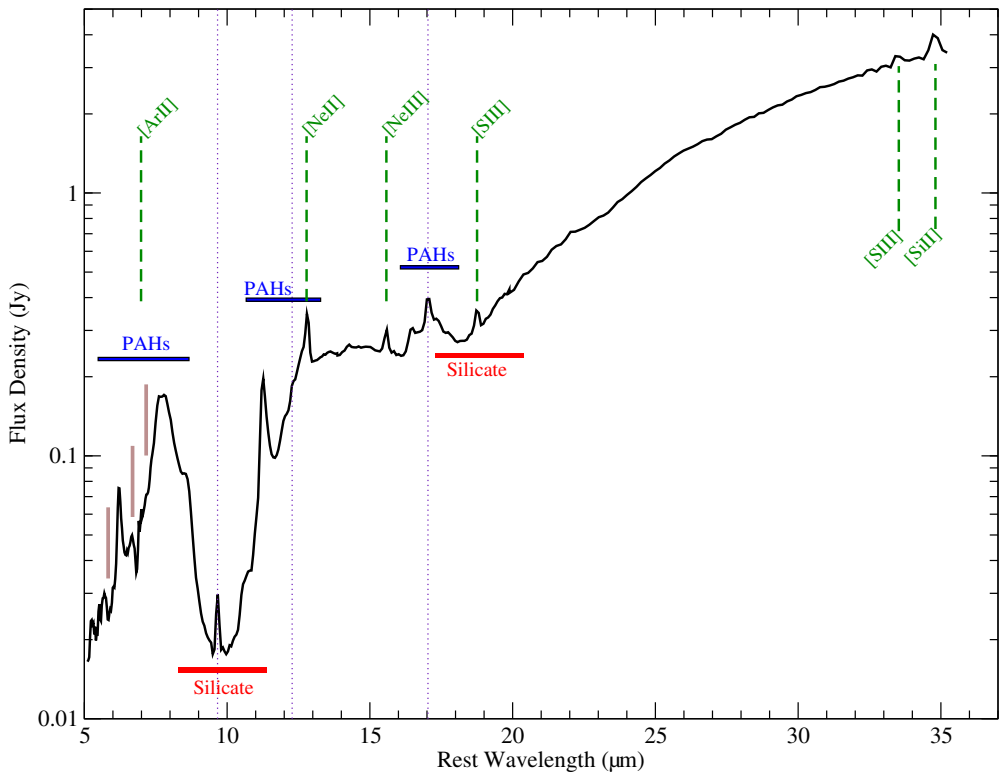

Figure 4. Low-resolution *Spitzer* IRS spectrum of the IRAS16399−0937 system, extracted from a circular aperture of radius 7″. The dotted lines indicate the positions of the H_2 $S(3)$ 9.66 μm, H_2 $S(2)$ 12.27 μm, and H_2 S(1) 17.03 μm emission lines. The brown solid lines indicate absorption bands of water ice (∼6.0 μm) and HACs (∼6.85 μm and 7.25 μm). The PAH and silicate features, as well as various ionic emission lines, are labeled.

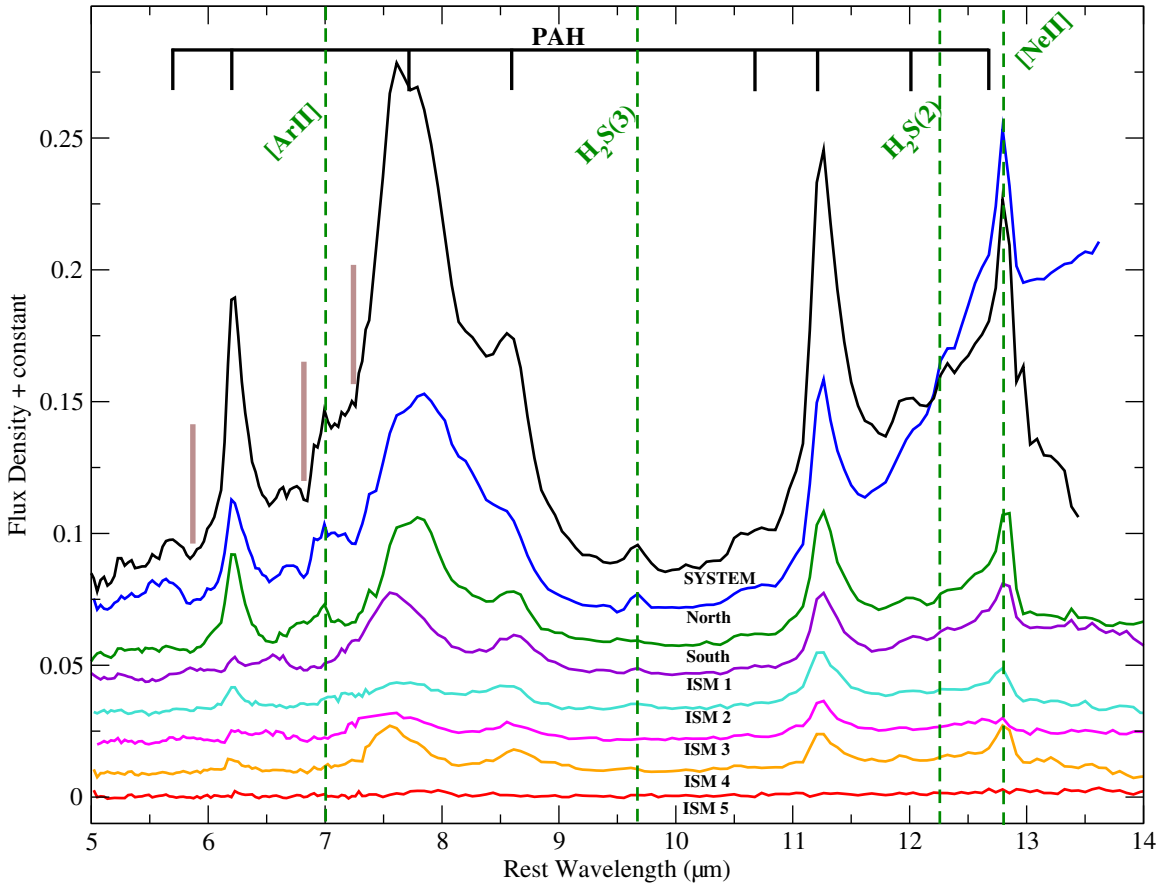

Figure 5. Low-resolution (SL module) IRS spectra of IRAS16399−0937. The integrated spectrum of the system (labeled SYSTEM), extracted from an aperture of radius 7″ is shown, along with spectra extracted from the apertures shown in Figure 3 centered on the IRAS16399N and IRAS16399S nuclei, as well as several locations in the extended envelope (ISM 1–5). The PAH bands and emission lines are labeled. The vertical brown solid lines show the positions of the water ice (∼6.0 μm) and HAC (∼6.85 μm and 7.25 μm) absorption bands.

The mid-IR spectrum of IRAS16399−0937 was observed as part of program 30323 (Armus et al. 2009). The data were obtained using the Short-Low (SL), and Long-Low (LL) Infrared Spectrograph (IRS; Houck et al. 2004) modules, which cover the interval between 5 μm and 37 μm with a resolving power of 64–128. The widths of the SL, and LL slits correspond to, respectively, ≈1.9 kpc (3.″7), and 5.5 kpc (10.″7) for IRAS16399−0937. The raw data were reduced using the IRS pipeline version 18.18 at the Spitzer Science Center (SSC).[13] The spectra are background-corrected and bad-/hot-pixel-corrected. Rogue pixels were removed and replaced using IRSCLEAN software available from the SSC.

A one-dimensional spectrum of the entire IRAS16399−0937 system was extracted using the default parameters of the Gaussian extraction method of the SMART code (Higdon et al. 2004). However, we used the optimal extraction method (Lebouteiller et al. 2010)[14] within SMART to extract spectra at seven locations along the slit, with two apertures centered on the IRAS16399N and IRAS16399S nuclei, respectively, and the others sampling the extended envelope. Figure 3 shows the position of each extracted spectrum superposed on the 8.0 μm IRAC image. To extract spectra using the optimal method, we selected an aperture of radius 2.″02 while the spectrum of the entire system was obtained with an aperture of radius 7″. The spectra were combined and order matched and are shown in Figures 4 and 5.

The IRS spectra were decomposed using the PAHFIT[15] code (Smith et al. 2007). This code assumes that the mid-IR spectrum is composed of dust continuum, starlight, prominent emission lines, individual and blended polycyclic aromatic hydrocarbon (PAH) emission bands, and that the light is attenuated by extinction due to silicate grains. The fluxes and equivalent widths (EWs) of spectral features properties derived from PAHFIT code are given in Tables 4 and 5. The PAHFIT decomposition of the IRAS16399−0937 system aperture is presented in Figure 6.

2.3. Herschel Data Reduction

The SPIRE photometric observations were made in the small-map mode (appropriate for fields smaller than 4 arcmin × 4 arcmin) on 2011 September 22 (PI: D. Sanders, ObsID: 1342229188). The SPIRE photometer (Griffin et al. 2010), with a field of view of 4 arcmin × 8 arcmin, is capable of carrying out simultaneous observations in three spectral bands, PSW (250 μm), PMW (350 μm) and PLW (500 μm), providing resolutions of about 18″, 25″, and 36″, respectively.

[13] http://ssc.spitzer.caltech.edu/irs/features/

[14] Lebouteiller et al. (2010)'s optimal extraction algorithm reduces the impact of noise from pixels containing little flux from the source and substantially improves the signal-to-noise ratio compared to spectra extracted with more conventional algorithms.

[15] Source and documentation of PAHFIT are available in http://tir.astro.utoledo.edu/jdsmith/research/pahfit.php.

Table 1
Photometric Properties of IRAS16399−0937

Filter	System Aperture $r = 7''$	IRAS16399N Aperture $r = 2''$	IRAS16399S Aperture $r = 2''$
$F_{\rm X-ray}^{0.5-2\,\rm keV}$ (erg s^{-1} cm^2)	$1.18 \pm 0.23 \times 10^{-13}$	$2.58 \pm 0.93 \times 10^{-14}$	$6.15 \pm 4.02 \times 10^{-15}$
Hα (erg s^{-1} cm^2)	5.79–17.4 $\times$ 10^{-13}	$1.80 \pm 0.26 \times 10^{-13}$	$1.00 \pm 0.14 \times 10^{-13}$
F435W (erg s^{-1} cm^2 Å^{-1})	$6.57 \pm 0.98 \times 10^{-16}$	$8.54 \pm 1.27 \times 10^{-17}$	$1.26 \pm 0.18 \times 10^{-16}$
F814W (erg s^{-1} cm^2 Å^{-1})	$2.33 \pm 0.34 \times 10^{-15}$	$3.84 \pm 0.57 \times 10^{-16}$	$4.50 \pm 0.67 \times 10^{-16}$
F914M (erg s^{-1} cm^2 Å^{-1})	$2.33 \pm 0.35 \times 10^{-15}$	$3.78 \pm 0.56 \times 10^{-16}$	$4.82 \pm 0.72 \times 10^{-16}$
1.2 μm (mJy) 2MASS	23.4 ± 3.5	2.53 ± 0.37	5.23 ± 0.78
1.6 μm (mJy) NICMOS	36.4 ± 5.44	4.23 ± 0.63	5.17 ± 0.77
2.1 μm (mJy) 2MASS	36.5 ± 5.46	4.60 ± 0.68	5.15 ± 0.77
3.6 μm (mJy) IRAC	18.42 ± 2.75	3.85 ± 0.57	3.88 ± 0.58
4.5 μm (mJy) IRAC	15.27 ± 2.28	4.14 ± 0.61	2.82 ± 0.42
5.8 μm (mJy) IRAC	49.78 ± 7.44	12.55 ± 1.87	7.56 ± 1.13
8.0 μm (mJy) IRAC	156.9 ± 23.47	34.03 ± 5.09	24.14 ± 3.61
ISM-dust 8.0 μm (mJy)	152.6 ± 22.82	33.14 ± 4.95	23.23 ± 3.47
24 μm (mJy) MIPS	486.33 ± 72.75	...	...
70 μm (Jy) MIPS	5.78 ± 0.86	...	...
160 μm (Jy) MIPS	2.241 ± 0.33	...	...
250 μm (Jy) SPIRE[a]	4.14 ± 0.3	...	...
350 μm (Jy) SPIRE[a]	1.00 ± 0.18	...	...
500 μm (Jy) SPIRE[a]	0.39 ± 0.13	...	...
1.49 GHz (Jy)[b, c]	$3.47 \pm 0.02 \times 10^{-2}$	$1.53 \pm 0.01 \times 10^{-2}$	$6.8 \pm 0.32 \times 10^{-3}$

Notes. IRAS16399N and System apertures were centered at R.A.:$16^{\rm h}42^{\rm m}40\overset{\rm s}{.}18$ and decl.:$-09^{\rm d}43^{\rm m}13\overset{\rm s}{.}26$. IRAS16399S was taken as R.A.:$16^{\rm h}42^{\rm m}40\overset{\rm s}{.}15$ and decl.:$-09^{\rm d}43^{\rm m}19\overset{\rm s}{.}02$.
[a] The photometry aperture used to measure the fluxes taken from *Herschel*/SPIRE images were $r = 36''$.
[b] The AIPS Gaussian-fitting task JMFIT was used to obtain these values. The beam-deconvolved sizes of the IRAS16399N and IRAS16399S components were $1\overset{''}{.}1 \times 0\overset{''}{.}5$ and $2\overset{''}{.}07 \times 1\overset{''}{.}3$, respectively.
[c] The AIPS verbs TVWIN+IMSTAT were used to obtain the total flux density value for a box region of size $14'' \times 14''$.

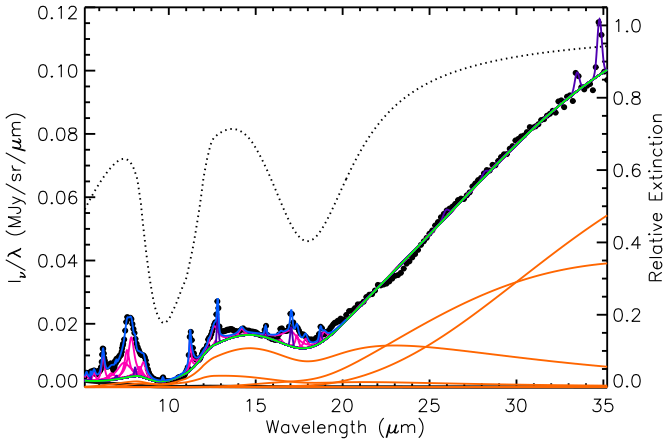

Figure 6. Result of the PAHFIT decomposition of the combined (SL+LL) IRS spectrum of the whole IRAS16399−0937 system. The data points are represented by filled circles, with uncertainties plotted as vertical error bars that are smaller than the symbol sizes. The best fit model is represented by the blue line. The dotted black line indicates the mixed extinction components, while solid green and orange lines represent total and individual thermal dust continuum components, respectively. The violet lines represent the ionic and hydrogen molecules, while the magenta lines represent PAH features.

We reduced the data using the *Herschel* Interactive Processing Environment (HIPE; Ott 2010) version 9.0 CIB 3071 (equivalent of HIPE 9.1.0). We used the simplified version of the small-map mode POF10 pipeline script and the naíve mapping algorithm. We did not include the turnarounds at the end of the scan lines in the processing and mapmaking procedures. Of the additional options available, we made maps with and without applying the relative bolometer gain corrections (useful for extended sources), and using both the baseline subtraction method (which removes baseline from the scans individually) and the destriper method (which subtracts a median baseline from all the scans), separately. The resulting flux densities were consistent within uncertainties.

The data processing was commenced from level 0.5 products—the SPIRE pointing product was created, the wavelet deglitcher was applied on the timeline data, the temperature drift correction was performed, and maps were created, the units of which were Jy beam^{-1}. The flux densities were measured by integrating the source counts within a circular aperture of radius $36''$. The sky background was calculated by placing a circular aperture at a region far removed from the source and subtracting the mean background flux from each pixel of the source aperture. Due to the non-uniformity of the sky background, we determined an average using three different locations. The flux measurements are given in Table 1.

2.4. VLA Radio Data

IRAS16399−0937 was observed at 1.49 GHz in the VLA A-array configuration on 1990 March 7 (Project code: AM293). These are unreduced data that were obtained from the NRAO archive[16] and processed with the Astronomical Image Processing System (AIPS) software using the standard calibration technique. The final radio image (Figure 1) was made after several iterations of phase and amplitude self-calibrations using the AIPS tasks CALIB and IMAGR. The final resultant rms noise in the image was $\sim 7 \times 10^{-5}$ Jy beam^{-1}. The radio image shows the presence of an unresolved core centered on the IRAS16399N

[16] https://archive.nrao.edu/

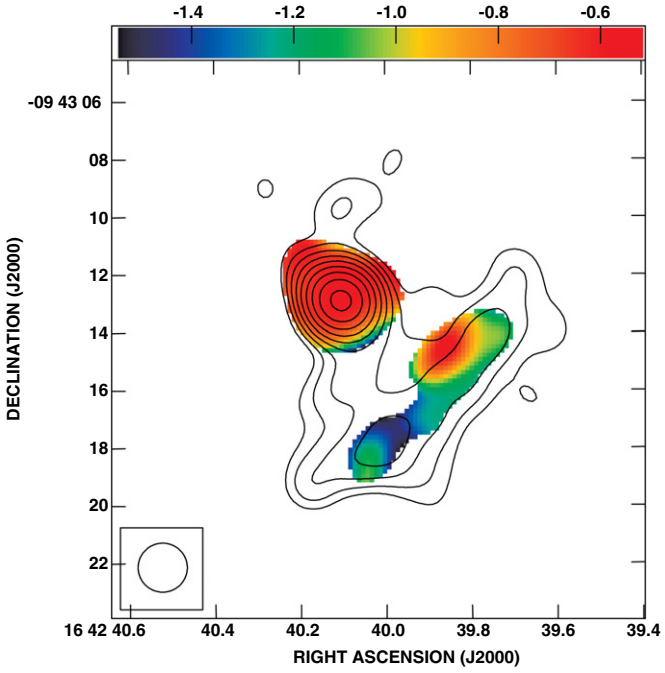

Figure 7. Radio spectral index image of IRAS16399−0937, derived from 1.49 and 4.9 GHz VLA images (see text). The 1.49 GHz emission contours are superposed. The contour levels are given in percentage of the peak intensity ($I_{\rm peak}$ = 12.9 mJy beam^{-1}) and increase by a factor of $\sqrt{2}$, with the lowest contour levels being equal to ±5.6%. The convolved beam size is 1.″7 × 1.″7.

nucleus. There is additional radio emission associated with the merging galaxy to the south. Table 1 shows the 1.4 GHz fluxes for the entire IRAS16399−0937 system, as well as for apertures centered on the IRAS16399N and IRAS16399S nuclei.

We combined the 1.49 GHz image with another data set extracted from the NRAO archive, a pipeline-reduced 4.9 GHz VLA A-array image (Project code: AB660),[17] to create a 1.49–4.9 GHz spectral index image (Figure 7). For the 4.9 GHz image, UVRANGE was restricted to 0–180 kλ in the task IMAGR and a UVTAPER of 150 kλ,0 was used. Both images were convolved with an intermediate-sized circular beam of 1.″7 × 1.″7, and aligned with the task OGEOM before creating the spectral index map using the task COMB. The spectral index, α, is defined such that flux density S_ν at frequency ν is $S_\nu \propto \nu^\alpha$.

2.5. Chandra X-Ray Image

The X-ray image of IRAS16399−0937 was extracted from the *Chandra* public data archive. The image was observed with *Chandra* on 2013 June 30 (ObsID 15055) using the focal plane detector ACIS-S operated in VFAINT imaging mode. This data set is part of the *Chandra* component of the Great Observatories All-sky LIRG Survey (Armus et al. 2009) program 14700854 (PI: D. Sanders). The exposure time of the image is 14.87 ks. The data were reduced with the standard *Chandra* data analysis package CIAO 4.6 with the latest calibration files in CALDB 4.6.1, and the script "srcflux" in CIAO to estimate the flux. The flux and luminosity derived for the whole system IRAS16399−0937, as well as for the two nuclei, IRAS16399N and IRAS16399S, are presented in Tables 1 and 2. Figure 8 shows a composite of the 1.49 GHz radio and X-ray images.

[17] https://archive.nrao.edu/archive/archiveimage.html

3. RESULTS

3.1. Optical to Near-IR Features

3.1.1. Morphology

The ACS medium- and broad-band images are presented in Figure 1, along with the continuum-subtracted Hα+[N II] emission line image. These show IRAS16399−0937 to be a merger system in which two galaxy cores (the IRAS16399N and IRAS16399S nuclei) reside in a highly disturbed common envelope. As already noted, the IRAS16399N (centered at R.A.: $16^{\rm h}42^{\rm m}40\overset{\rm s}{.}18$ and decl.: $-09^{\rm d}43^{\rm m}13\overset{\rm s}{.}26$) and IRAS16399S (centered at R.A.: $16^{\rm h}42^{\rm m}40\overset{\rm s}{.}15$ and decl.: $-09^{\rm d}43^{\rm m}19\overset{\rm s}{.}02$) nuclei have been classified as a LINER and a starburst, respectively, based on their optical spectra (Baan et al. 1998). The two nuclei are separated by a projected distance of ∼6″ (3.4 kpc). Extensive dust lanes interpenetrate the region between the two nuclei and extend several arcseconds across the system to the east and west.

The IRAS16399N nucleus is the more compact of the two, but it is crossed by a dust lane that is clearly visible in the broadband F435W image (Figure 2). The IRAS16399S nucleus has a more extended and disturbed morphology. In addition to the nuclei, two other main morphological features are prominent in the blue (F435W) continuum emission (Figure 1). An arc-like structure, loops around the system to the west, connecting the IRAS16399S nucleus to a large amorphous region of emission that extends ∼3 kpc to the north and east of the IRAS16399N nucleus (Figure 1). Hereafter, we refer to these features as the "western arc" and the "northeastern blob," respectively.

Line emission in Hα+[N II] is widely distributed around the system, with bright knots embedded in more diffuse patches associated with the main morphological features apparent in the continuum images, including both nuclei, the northeastern blob, and the western arc. In addition, a smaller arc of ionized gas emerges from the north west side of the IRAS16399N nucleus and curves back in a north-easterly direction. The line emission associated with the IRAS16399S nucleus is extended and patchy, while that associated the IRAS16399N nucleus is more concentrated. Strings of knots are visible in both the Hα+[N II] and the continuum images (e.g., NW of the IRAS16399S nucleus and NE of the IRAS16399N nucleus). Given that the *B* band (F435W) and Hα+[N II] emission trace, respectively, young stars and H II regions, it is clear that recent or ongoing (and relatively unobscured) star formation, while concentrated in the structures mentioned above, is widespread across the envelope over scales of several kiloparsecs.

The 1.6 μm emission, mapped in the NICMOS F160W image, is less sensitive to dust extinction and predominantly traces the old stellar population, providing a clearer picture of the stellar mass distribution, which can be compared with the gas and dust morphology. Although the overall morphology of the system at 1.6 μm is similar to that seen in the optical images, the two nuclei dominate and are much more clearly defined, appearing as approximately elliptical structures with compact central cores. The IRAS16399S nucleus, however, also has a prominent spur pointing NW, which is clearly associated with the base of the western arc. Several of the brighter knots (H II regions) are also prominent at 1.6 μm. The same features appear in the Near-IR *J* and *K* band images obtained from the Two Micron All Sky Survey (2MASS) data archive.

IRAS16399−0937 was included in the sample of (U)LIRGs studied by Haan et al. (2011), who classify it as a

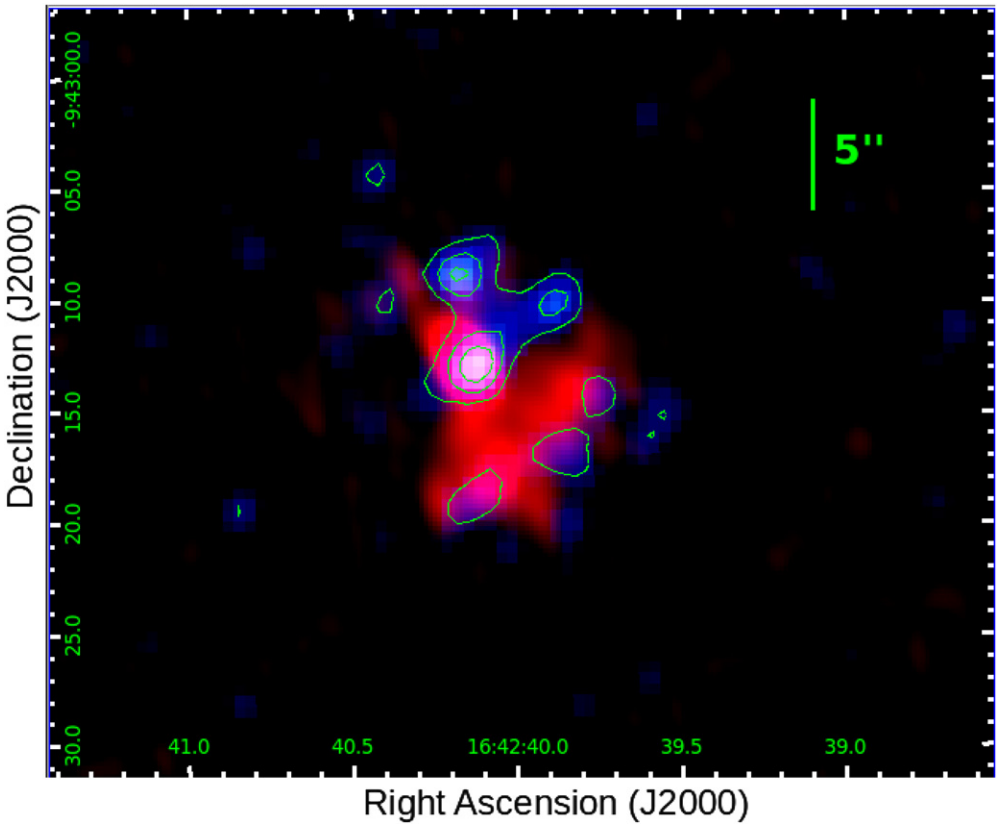

Figure 8. Composite image of IRAS16399−0937. The red and blue channels represent the 1.49 GHz VLA and *Chandra* X-ray, respectively. The contours show the X-ray emission (contours are linear and stepped in 25% increments of the peak). The X-ray image was smoothed with a Gaussian function with $\sigma = 3$ pixels.

Table 2
Luminosity in IRAS16399−0937

Filter	System Aperture $r = 7''$	IRAS16399N Aperture $r = 2''$	IRAS16399S Aperture $r = 2''$
$L_{\rm X-ray}^{0.5-2\,{\rm keV}}$ (erg s^{-1})	$2.14 \pm 0.41 \times 10^{41}$	$4.69 \pm 1.69 \times 10^{40}$	$1.12 \pm 0.73 \times 10^{40}$
$L_{\rm H\alpha}$ (erg s^{-1})	1.05–3.16 $\times$ 10^{42}	$3.27 \pm 0.47 \times 10^{41}$	$1.81 \pm 0.25 \times 10^{41}$
$\nu L_{8.0\mu\,{\rm m,dust}}$ (erg s^{-1})	$1.04 \pm 0.15 \times 10^{44}$	$2.25 \pm 0.37 \times 10^{43}$	$1.58 \pm 0.23 \times 10^{43}$
$\nu L_{24\mu\,{\rm m,dust}}$ (erg s^{-1})	$1.10 \pm 0.16 \times 10^{44}$	...	...
$\nu L_{1.49\,{\rm GHz}}$ (erg s^{-1})	$9.40 \pm 0.54 \times 10^{38}$	$4.14 \pm 0.38 \times 10^{38}$	$1.84 \pm 0.28 \times 10^{38}$

mid-stage merger (stage 3: two nuclei in a common envelope, according to their classification scheme) based on *HST*/ACS *B*- and *I*-band images. Haan et al. also modeled the surface brightness distribution in an *HST*/NICMOS *H*-band image, using a combination of two Sérsic profiles. Notably, a point source was also required to fit the IRAS16399N nucleus. From the decomposition, Haan et al. find that the two nuclei have very similar *H*-band luminosities $\log(L_{\rm bulge}/L_\odot) \approx 10.6$, but the IRAS16399S nucleus is more compact ($R_{\rm bulge} \approx 0.5$ kpc, compared to $\approx$1 for the IRAS16399N nucleus) and therefore has a higher luminosity density ($L_{\rm bulge}/R_{\rm bulge}^2$). The Sérsic indices also differ, indicating radial brightness profiles consistent with a disk-like pseudo-bulge in the IRAS16399N nucleus ($n_s \approx 1.3$) and a classical bulge ($n_s \approx 2.9$) in the IRAS16399S nucleus, respectively (Fisher & Drory 2008), suggesting that the progenitor galaxies followed different evolutionary paths (e.g., Kormendy & Kennicutt 2004). Haan et al. also derived black hole masses from the *H*-band luminosities using Marconi & Hunt's (2003) relation, finding $M_{\rm BH} \approx 10^8\ M_\odot$ for both nuclei.[18]

3.1.2. Hα Photometry

Emission line fluxes were measured from the continuum subtracted FR656N ramp filter image using circular apertures of radius 2.″02 centered on the IRAS16399N and IRAS16399S nuclei, respectively. A circular aperture of radius 7.″0 was used to measure the total emission line flux of the whole system.

As the FR656N ramp filter includes both Hα and the [N II] $\lambda\lambda$6548, 83 lines in its passband, it is necessary to correct for both dust extinction and the contribution of the [N II]

[18] It should be noted, however, that recent work suggests that pseudo-bulges may not follow the same scaling relationships with black hole mass as classical bulges and elliptical galaxies (e.g., Kormendy et al. 2011). Marconi & Hunt (2003) do not distinguish between bulge types, but their sample is dominated by ellipticals and lenticulars.

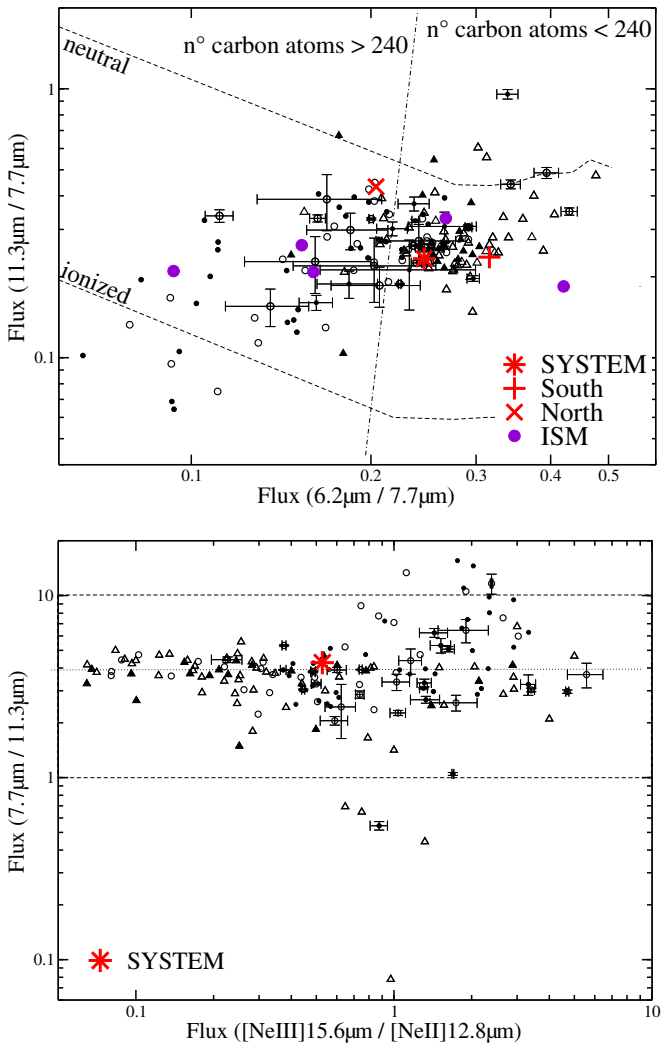

Figure 9. Comparison of IRAS16399−0937 regions with galaxies exhibiting starburst activity or AGN in mid-IR diagnostic diagrams. Top panel: 6.2 μm/7.7 μm vs. 11.3 μm/7.7 μm PAH flux ratios. The dashed lines represent theoretical loci for neutral and ionized PAHs (Draine & Li 2001). The dot-dash line shows the locus of molecules formed by 240 carbon atoms. Points representing the integrated spectrum of the IRAS16399−0937 system, the IRAS16399N and IRAS16399S nuclei and the ISM sub-regions are plotted using the symbols shown in the key. Bottom panel: 7.7 μm/11.3 μm PAH flux ratio plotted vs. [Ne III] 15.5/[Ne II] 12.8 μm. This diagram is used as an indicator of the hardness of the radiation field (e.g., Smith et al. 2007; Sales et al. 2010; Baum et al. 2010). As the [Ne III] 15.5 μm line falls in the IRS LL spectrum, which does not resolve the two nuclei, or the ISM sub-regions, only the point representing the integrated spectrum of IRAS16399−0937 is plotted in this diagram. In both panels, the galaxy data are taken from the sample compiled by (Sales et al. 2010; see also Smith et al. 2007; Brandl et al. 2006; Gallimore et al. 2010): empty triangles represent H II galaxies and LINERs; filled triangles are starburst galaxies; filled and empty circles are Seyfert 1 and 2 galaxies, respectively.

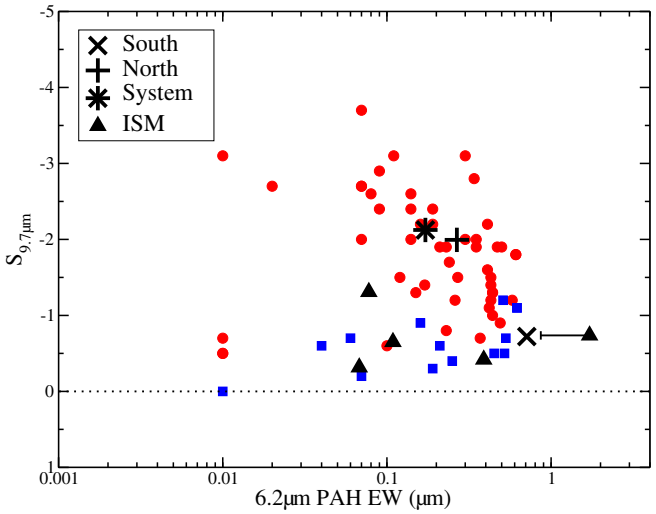

Figure 10. Comparison of IRAS16399−0937 regions in "fork" diagram of 6.2 μm PAH EW vs. the silicate optical depth at 9.7 μm. Points representing the integrated spectrum of the IRAS16399−0937 system, the IRAS16399N and IRAS16399S nuclei and the ISM sub-regions are plotted using the symbols shown in the key. OHMGs from the sample of Willett et al. (2011a) are shown in red circles and the non-OHMGs are shown in blue squares. For derived errors, see Tables 4 and 5.

lines in order to estimate the intrinsic Hα fluxes. Approximate corrections can be derived from the optical line intensities published by Baan et al. (1998) and Kewley et al. (2001), both of whom obtained long-slit spectra crossing both nuclei. However, while most of the line intensity ratios given in these studies agree to within 20%–30%, there is serious disagreement as to the reddening corrections derived from the Hα/Hβ ratio. The reddening estimated by Baan et al. implies extinctions at Hα of $A_{\rm H\alpha} \approx 5.9$ ($A_V \approx 6.8$) and 3.0 ($A_V \approx 3.4$) mag for the IRAS16399N and IRAS16399S nuclei, respectively, whereas Kewley et al.'s results imply $A_{\rm H\alpha} \approx 3.2$ ($A_V \approx 3.8$) and 2.0 ($A_V \approx 2.4$) mag. For the IRAS16399N nucleus, in particular, the difference in $A_{H\alpha}$ of ≈3 mag corresponds to an order of magnitude in the intrinsic flux after correcting for extinction. While there is no compelling reason to favor either extinction estimate, the extraction aperture used by Kewley et al. (1 kpc, corresponding to ≈2″ at the redshift of IRAS16399−0937) is approximately the same size as our own, whereas that used by Baan et al. was ≈3× larger and must therefore include emission from the regions surrounding each nucleus. In the following, therefore, we adopt the extinction and line ratios given by Kewley et al., on the grounds that they are more likely to represent reasonable average values for the two nuclei. Nevertheless, we note that if Baan et al.'s results are used, the Hα luminosities of the IRAS16399N and IRAS16399S nuclei increase by factors of 11 and 2.4, respectively.

We first correct the measured emission line fluxes for extinction using the selective extinction given by Kewley et al. for each nucleus and the standard Milky Way reddening curve ($R_V = 3.1$). The reddening corrected [N II λ6583]/Hα ratios from Kewley et al. were then used to estimate the Hα contribution to the total Hα + [N II] λλ6548, 83 flux in each nuclear aperture. We find Hα contributions of ∼41% and ∼58% for the IRAS16399N and IRAS16399S nuclei, respectively, yielding dereddened Hα fluxes of 1.8×10^{-13} erg s^{-1} cm^{-2} and 1.0×10^{-13} erg s^{-1} cm^{-2} (Table 1).

As optical spectroscopy is available only for the nuclei, we have no direct measurement of the average extinction or [N II λ6583]/Hα ratio for the extended emission line regions pervading the envelope. However, as the extended line emission is probably dominated by star formation, we adopt the value of [N II]/Hα for the IRAS16399S nucleus (which has line ratios characteristic of H II regions; Baan et al. 1998; Yuan et al. 2010; see Section 5) and estimate the total Hα flux using the values of $A_{H\alpha}$ derived for the IRAS16399N and IRAS16399S nuclei as upper and lower limits, respectively, for the extinction. This yields, a total Hα flux for the whole system in the range $F_{\rm H\alpha} \approx 5.8$–$17.4 \times 10^{-13}$ erg s^{-1} cm^{-2} (Table 1).

Table 3
Star Formation Rates in IRAS16399−0937

Filter	System Aperture $r = 7''$	IRAS16399N Aperture $r = 2''$	IRAS16399S Aperture $r = 2''$
$SFR^{0.5-2\,keV}_{X-ray}$ ($M_\odot$ yr^{-1})	47.08 ± 9.02	10.32 ± 3.72	2.46 ± 1.60
$SFR_{H\alpha}$ ($M_\odot$ yr^{-1})	5.58−16.76	1.73 ± 0.25	0.96 ± 0.14
$SFR_{8.0\mu m,dust}$ ($M_\odot$ yr^{-1})	19.37 ± 2.89	4.21 ± 0.63	2.95 ± 0.44
$SFR_{24\mu m,dust}$ ($M_\odot$ yr^{-1})	23.18 ± 3.16	...	...
$SFR_{1.49\,GHz}$ ($M_\odot$ yr^{-1})	13.72 ± 1.46	6.04 ± 0.65	2.68 ± 0.21

As the Hα luminosity produced by a star forming region is proportional to the global rate of production of ionizing photons, it can be related to the total SFR over all stellar masses. We adopt the following relation, from Calzetti et al. (2007):

$$SFR_{H\alpha}(M_\odot\,yr^{-1}) = 5.3 \times 10^{-42}\, L_{(H\alpha,corr)}, \quad (1)$$

where $L_{(H\alpha,corr)}$ is the Hα luminosity in erg s^{-1}. For the IRAS16399N and IRAS16399S nuclei, the reddening-corrected Hα fluxes imply $SFR_{H\alpha}$ of $\sim$1.73 $M_\odot$ yr^{-1} and $\sim$0.96 $M_\odot$ yr^{-1}, respectively (see Tables 2 and 3). It should be noted, however, that as the IRAS16399N nucleus has a LINER spectrum (Baan et al. 1998; Yuan et al. 2010; see Section 5), its Hα emission is likely to include a large contribution due predominantly to processes other than stellar photoionization. The derived SFR should therefore be regarded as an extreme upper limit.

The global SFR implied by the total $H\alpha$ luminosity of the whole system ($7''$) is $SFR_{H\alpha} \sim 5.58$–$16.76\ M_\odot$ yr^{-1} (Table 1).

3.2. The Mid- to Far-IR Features

3.2.1. Mid-IR Spectroscopy

The mid-IR spectral range is very rich in emission features of molecular gas, such as H_2, PAH, and silicate bands (Puget & Leger 1989; Genzel et al. 1998; Draine 2003). Prominent ionic emission lines of neon, oxygen, sulfur, and silicon are also present (e.g., Genzel et al. 1998; Sturm et al. 2002; Gallimore et al. 2010; Sales et al. 2010). The observed spectrum of the entire IRAS16399−0937 merger system (Figure 4) clearly shows prominent emission from the well-known PAH bands at 6.2, 7.7, 8.6, 11.3, and 12.7 μm, as well as molecular hydrogen lines due to vibrational modes at 5.5, 6.9, 8.0, 9.6, 12.2, and 17.0 μm. In addition, the mid-IR spectrum exhibits emission lines due to ions of moderate ionization potential (IP < 50 eV), such as [Ne II] 12.8 μm, [Ne III] 15.5 μm, [S III] 18.7 μm and 33.48 μm, and [Si II] 34.8 μm. However, IRAS16399−0937 does not show the higher ionization lines ([Ne V] at 14.3 μm and 24.2 μm or [Ne VI] at 7.6 μm) that are often taken as indicators of the presence of the hard radiation field (IP > 90eV) associated with an AGN (Genzel et al. 1998; Sturm et al. 2000; Armus et al. 2007). The PAH and emission line fluxes are listed in Table 4.

Absorption bands arising from the water ice stretching mode at 6.0 μm and from hydrogenated amorphous carbon (HAC) grains at 6.85 and 7.25 μm (see also Chiar et al. 2000; Dartois et al. 2007) are also clearly present. While the water ice absorption band is an indicator of a heavily extincted and enshrouded nucleus, AGN, or starburst (Spoon et al. 2001), the HAC features are known to be associated with dust in the diffuse interstellar medium (ISM). Such features are commonly observed in LIRGs and ULIRGs (Spoon et al. 2001, 2002; Willett et al. 2011a). According to Willett et al. (2011a, 2011b), both water ice and HAC features are common in OHMGs, having been detected in 50% of their sample of 51 OHMGs. The ice and HAC optical depths were measured by adjusting a spline continuum to the average fluxes within 1 μm windows with pivots at 5.2, 5.6, 7.8, and 13.5 μm (Spoon et al. 2007; Willett et al. 2011a) and taking the ratio between observed and continuum fluxes of these absorption features (see Table 4).

In order to investigate the spatial variation of the mid-IR emission features in IRAS16399−0937, we extracted SL (5.2–14μm) spectra from seven regions along the slit (Figure 3), including the two nuclei and five contiguous locations in the extended envelope, one between the two nuclei (ISM 1), three north of nucleus N (ISM 2–4) and one south of nucleus IRAS16399S (ISM 5). The extracted spectra are shown in Figure 5. The spectrum of the IRAS16399N nucleus exhibits the same ionic and molecular emission lines as those present in the integrated spectrum of the entire system. It shows deeper ice and HAC absorption bands than the integrated spectrum, or indeed those of the IRAS16399S nucleus and ISM regions. These features may indicate the presence of dense and cold material in the IRAS16399N nucleus. However, the most striking difference between the IRAS16399N nucleus spectrum and the spectra obtained from the other apertures is the steep rise in the continuum to wavelengths $\gtrsim 12\mu$m, which implies that an additional component of warm dust ($\sim$100 K) contributes strongly to the IR emission from this region. This rise in the spectrum at longer wavelengths is consistent with the composite NICMOS F160W and MIPS 24 μm image presented by Haan et al. (2011), which shows that the IRAS16399N nucleus dominates the 24 μm emission from the merger system.

The mid-IR spectrum (5–14 μm) of the IRAS16399S nucleus shows strong PAH emission bands similar to those of the IRAS16399N nucleus. However, the emission lines of [Ne II] at 12.8 μm, and H_2 at 9.6 μm, as well as the water ice and HAC absorption bands are fainter than in the IRAS16399N nucleus. While the ISM 1 spectrum shows prominent PAH bands, but fainter ice and HAC absorption bands compared to the IRAS16399N and IRAS16399S nuclei, the ISM 2, 3, and 4 extractions show relatively weak PAH emission and no molecular absorption features.

Draine & Li (2001) pointed out that the strengths of the PAH bands at 6.2 μm, 7.7 μm, 8.6 μm, and 11.3 μm depend on the size and on the charge state of the molecules (see also, Draine 2003; Tielens 2008; Peeters et al. 2002). and proposed a diagnostic diagram based on the PAH emission ratios 6.2 μm/7.7 μm and 11.3 μm/7.7 μm, which are sensitive to the size and ionization state, respectively, of these molecules (Draine & Li 2001; Li & Draine 2001). Sales et al. (2010) used that diagram to argue that AGNs exhibit higher ionization fractions and larger PAH molecules than starburst galaxies and proposed that PAH ratios can therefore distinguish star-forming galaxies from AGNs. It has also been suggested by several authors that the ratio of the [Ne II] 12.8 μm and [Ne III] 15.5 μm lines, compared to the relative strengths of PAH bands, can be used to classify the mid-IR spectra of galaxies according to the nature of the ionizing source (e.g., Smith et al. 2007; Sales et al. 2010; Baum et al. 2010).

In Figure 9, we plot the measured values of the PAH 6.2 μm/7.7 μm and 11.3 μm/7.7 μm ratios for the extracted spectra as well as the spectrum of the IRAS16399−0937 system. We also include data from the sample compiled by Sales et al. (2010) representing H II galaxies, starburst galaxies, LINERs and Seyfert 1 and 2 galaxies. The point representing the system spectrum of IRAS16399−0937 falls in the region populated with a mix of Seyfert and starburst galaxies (Sales et al. 2010), while the IRAS16399N and IRAS16399S nuclei

Table 4
Mid-Infrared Emission Line Strengths (10^{-17} W m^2) and Equivalent Widths (μm)

Line	System		IRAS16399N		IRAS16399S	
	Flux	EW	Flux	EW	Flux	EW
H_2 *a*S(7) 5.5 μm	10.7 ± 5.13	0.073	12.7 ± 0.733	0.165	1.57 ± 0.275	0.106
H_2 *S*(5) 6.9 μm	<2.65	0.016	4.06 ± 0.406	0.035	3.41 ± 0.220	0.169
[Ar II] 6.99 μm	<5.37	0.032	8.50 ± 0.471	0.073	5.47 ± 0.216	0.268
H_2 S(4) 8.0 μm	21.7 ± 18.9	0.140	15.0 ± 0.5.97	0.132	...	...
[Ar III] 8.9 μm	<8.73	0.129	3.51 ± 0.994	0.084	1.10 ± 0.151	0.052
H_2 S(3) 9.6 μm	42.4 ± 10.4	0.917	38.0 ± 9.56	1.41	0.799 ± 0.09	0.038
[S IV] 10.5 μm	<3.43	0.047	4.59 ± 0.744	0.116	0.751 ± 0.107	0.035
H_2 S(2) 12.2 μm	<4.77	0.017	3.98 ± 0.217	0.024	1.03 ± 0.115	0.033
[Ne II] 12.8 μm	41.6 ± 16.1	0.132	24.9 ± 3.15	0.122	9.62 ± 1.67	0.261
[Ne V] 14.2 μm	<4.92	0.013	...	...	...	...
[Ne III] 15.5 μm	9.29 ± 1.35	0.029	...	...	...	...
H_2 *S*(1) 17.0 μm	55.0 ± 28.6	...	...	...	...	...
[S III] 18.7 μm	29.4 ± 19.6	0.134	...	...	...	...
[O IV] 25.8 μm	<9.77	0.015	...	...	...	...
[Fe II] 26.0 μm	<9.05	...	...	...	...	...
H_2 S(0) 28.1 μm	<16.4	0.023	...	...	...	...
[S III] 33.4 μm	<16.2	0.019	...	...	...	...
[Si II] 34.7 μm	<4.51	0.052	...	...	...	...
PAH features						
6.2 μm	217 ± 23.2	0.953	183 ± 23.2	1.28	92.5 ± 9.23	3.45
7.4 μm[a]	365 ± 107	1.52	188 ± 10.9	1.07	61.9 ± 3.34	2.00
7.6 μm[a]	361 ± 95.6	1.49	281 ± 3.63	1.57	121 ± 1.55	3.90
7.8 μm[a]	575 ± 9.58	2.43	428 ± 31.4	2.45	110 ± 11.0	3.50
8.3 μm	117 ± 63.2	0.603	112 ± 26.8	0.827	19.5 ± 1.748	0.624
8.6 μm	322 ± 53.2	2.07	209 ± 26.0	2.12	54.3 ± 6.18	1.75
11.2 μm[b]	242 ± 51.4	1.43	180 ± 16.0	1.97	21.7 ± 3.35	0.636
11.3 μm[b]	205 ± 64.5	1.12	208 ± 25.4	2.11	47.6 ± 6.71	1.37
12.0 μm	<17.2	0.053	19.4 ± 1.58	0.105	24.7 ± 7.79	0.599
12.6 μm[c]	230 ± 78.5	0.520	124 ± 12.6	0.440	47.7 ± 7.82	0.932
12.7 μm[c]	<0.93	0.002	...	...	...	...
16.4 μm[d]	12.5 ± 3.72	0.032	...	...	...	...
17.0 μm[d]	377 ± 149	1.12	...	...	...	...
17.4 μm[d]	78.9 ± 44.1	0.253	...	...	...	...
17.9 μm[d]	84.2 ± 38.1	0.282	...	...	...	...
S_{sil}[e]	−2.12 ± 0.376		−2.06 ± 0.366		−0.75 ± 0.133	
$EW_{6.2\,\mu m}$[f]	0.171 ± 0.01		0.266 ± 0.01		0.711 ± 0.012	
$\tau_{9.7\,\mu m}$[g]	5.59 ± 0.017		5.1 ± 0.018		0.35 ± 0.002	
τ_{ice} 6.0 μm	0.729 ± 0.108		0.548 ± 0.081		0.279 ± 0.041	
τ_{HAC} 6.85 μm	0.909 ± 0.135		1.072 ± 0.160		0.723 ± 0.107	
τ_{HAC} 7.25 μm	0.519 ± 0.077		0.670 ± 0.100		0.685 ± 0.102	

Notes.
[a] 7.7 μm Complex.
[b] 11.3 μm Complex.
[c] 12.7 μm Complex.
[d] 17 μm Complex.
[e] Silicate apparent strength, $S_{sil} = \ln(f_{obs}/f_{cont})$, was derived using the method of Spoon et al. (2007); Willett et al. (2011a).
[f] Equivalent Width of 6.2 μm PAH derived using the same method of Spoon et al. (2007); Willett et al. (2011a).
[g] Silicate optical depth derived using PAHFIT (Smith et al. 2007).

are located in regions occupied by majority of the Seyfert and starburst galaxies, respectively. The ISM extractions are distributed widely over the diagram, such that the ISM 1, 3, and 4 are present in the region dominated by the Seyfert galaxies and ISM 2 and 5 are present in the region of starburst galaxies.

The ISM extractions that lie in the Seyfert region of the diagram are those from positions closest to the IRAS16399N nucleus, either between the two nuclei (ISM 1) or to the north (ISM 3 and 4; Figure 3). It is also worth noting that these ISM points have their 6.2 μm PAH emission suppressed (Table 5) relative to those that fall well within the starburst region. As possible explanation is that the small ($\leqslant$50 carbon atoms) PAHs are destroyed by shocks, with velocities greater than 100 km s^{-1} (Micelotta et al. 2010a, 2010b), caused by the merger interaction. In contrast, the ISM positions furthest away (ISM 2 and 5) from the IRAS16399N nucleus—those located near the north and south edges of the common envelope—fall in

Table 5
MIR Emission Line Strengths (10^{-17} W m^2) and Equivalent Widths (μm)

Line	ISM 1		ISM 2		ISM 3		ISM 4		ISM 5	
	Flux	EW	Flux	EW	Flux	EW	Flux	EW	Flux	EW
H_2 $S(5)$ 5.5 μm	...	...	...	...	...	...	...	...	0.70 ± 0.37	1.65
[Ar II] 6.9 μm	...	...	...	...	...	...	<0.04	0.008	0.33 ± 0.28	0.218
H_2 $S(4)$ 8.0 μm	0.62 ± 0.23	0.040	0.62 ± 0.23	0.040	<0.007	0.001	<0.12	0.023	0.53 ± 0.41	0.256
[Ar III] 8.9 μm	1.34 ± 0.19	0.114	1.34 ± 0.19	0.114	0.37 ± 0.17	0.074	1.05 ± 0.13	0.215	...	...
H_2 $S(3)$ 9.6 μm	1.14 ± 0.14	0.121	1.14 ± 0.14	0.121	...	...	0.39 ± 0.08	0.084	0.92 ± 0.55	0.977
[S IV] 10.5 μm	0.26 ± 0.15	0.024	0.26 ± 0.15	0.024	0.39 ± 0.14	0.075	0.50 ± 0.11	0.122	0.42 ± 0.36	0.343
H_2 $S(2)$ 12.27 μm	0.75 ± 0.15	0.039	0.75 ± 0.15	0.039	0.23 ± 0.14	0.040	0.38 ± 0.13	0.121	<0.06	0.025
[Ne II] 12.8 μm	4.21 ± 0.21	0.179	4.21 ± 0.21	0.179	0.36 ± 0.17	0.065	3.15 ± 0.17	1.08	0.21 ± 0.20	0.086
PAH features										
6.2 μm	15.3 ± 0.85	0.645	15.3 ± 0.85	0.645	8.88 ± 0.88	1.98	11.0 ± 0.74	1.46	3.31 ± 1.11	2.49
7.4 μm[a]	68.4 ± 3.53	2.86	68.4 ± 3.53	2.86	29.6 ± 4.77	4.46	20.7 ± 3.02	2.66	...	...
7.6 μm[a]	65.9 ± 1.79	2.77	65.9 ± 1.79	2.77	18.7 ± 1.78	2.74	43.0 ± 1.53	5.55	...	...
7.8 μm[a]	29.5 ± 1.29	1.27	29.5 ± 1.29	1.27	9.67 ± 1.36	1.35	4.96 ± 1.13	0.643	7.87 ± 1.42	2.6
8.3 μm	...	...	...	...	<0.26	0.035	...	...	...	...
8.6 μm	33.4 ± 0.72	1.69	33.4 ± 0.72	1.69	13.7 ± 0.794	1.81	16.0 ± 0.53	2.15	<0.91	0.344
11.2 μm[b]	11.5 ± 0.45	0.612	11.5 ± 0.45	0.612	5.78 ± 0.39	0.716	4.90 ± 0.33	0.889	...	...
11.3 μm[b]	22.9 ± 0.88	1.18	22.9 ± 0.88	1.18	9.42 ± 0.692	1.16	9.41 ± 0.54	1.73	1.45 ± 0.96	0.555
12.0 μm	9.33 ± 0.90	0.374	9.33 ± 0.90	0.374	3.54 ± 0.57	0.425	6.32 ± 0.45	1.29	...	...
12.6 μm[c]	21.7 ± 1.43	0.679	21.7 ± 1.43	0.679	8.25 ± 1.01	1	10.0 ± 0.93	2.27	<0.51	0.137
12.7 μm[c]	1.46 ± 0.51	0.044	1.46 ± 0.51	0.044	<0.17	0.0215	0.97 ± 0.43	0.222	<0.55	0.146
S_{sil}[e]	-1.31 ± 0.150		-0.41 ± 0.048		-0.31 ± 0.036		-0.65 ± 0.074		-0.73 ± 0.084	
$EW_{6.2\,\mu m}$[f]	0.077 ± 0.008		0.388 ± 0.044		0.067 ± 0.007		0.108 ± 0.012		1.715 ± 0.850	
$\tau_{9.7\,\mu m}$[g]	0.87 ± 0.099		<0.01		0.52 ± 0.059		<0.01		3.94 ± 1.27	
τ_{ice} 6.0 μm	0.273 ± 0.031		0.282 ± 0.032		0.805 ± 0.153		0.112 ± 0.02		<0.01	
τ_{HAC} 6.85 μm	0.137 ± 0.015		<0.05		1.664 ± 0.316		<0.1		<0.01	
τ_{HAC} 7.25 μm	0.131 ± 0.015		0.125 ± 0.014		0.248 ± 0.047		0.319 ± 0.040		<0.01	

Notes.
[a] 7.7 μm complex.
[b] 11.3 μm complex.
[c] 12.7 μm complex.
[d] 17 μm complex.
[e] Silicate apparent strength, $S_{sil} = ln\,(f_{obs}/f_{cont})$, was derived using the method of Spoon et al. (2007); Willett et al. (2011a).
[f] Equivalent width of 6.2 μm PAH derived using the same method of Spoon et al. (2007); Willett et al. (2011a).
[g] Silicate optical depth derived using PAHFIT (Smith et al. 2007).

the starburst region of the diagram (Sales et al. 2010; O'Dowd et al. 2009).

In Figure 9 we plot the 7.7 μm/11.3 μm PAH ratio versus [Ne II] 12.8 μm/[Ne III] 15.5 μm, again using data from the samples described by Sales et al. (2010). As the [Ne III] 15.5 μm line falls in the IRS LL spectrum, which does not resolve the two nuclei, we plot only one point for IRAS16399−0937, that for the integrated spectrum of the system. It can be seen that the IRAS16399−0937 merger system falls in the "transition" region of the diagram where there is most overlap between the populations of starburst galaxies and AGNs.

The well-known "fork diagram," which relates the optical depth of the silicate dust feature (S_{sil}) to the EW of the 6.2 μm PAH feature, provides another diagnostic of the relative strengths of AGNs and starburst activity in (U)LIRGs (Spoon et al. 2007). In this diagram galaxies appear to be systematically distributed along two distinct branches. The majority of ULIRGs are found along the upper branch, which appears to trace obscuration from optically identified starburst nuclei (strong PAH EW; weak silicate absorption) to deeply embedded nuclei (weak PAH EW, deep silicate absorption). The lower branch is characterized by weak silicate absorption and a range in PAH EW, and is occupied by AGNs (low EW) and starburst nuclei (high EW).

In Figure 10 we plot these quantities for the IRAS16399−0937 system, the two nuclei and the ISM regions, together with data for samples of OHM and non-OHM galaxies taken from Willett et al. (2011a). To be consistent with the measurement methodology used by the latter authors, we used a spline-fit to measure the EWs of the 6.2 μm PAH feature in IRAS16399−0937. Local continuum pivots were defined at 5.15, 5.55, 5.95, 6.55, and 7.1 μm and the integrated 6.2 μm PAH flux was divided by the continuum flux density obtained from the spline fit at the peak wavelength of the PAH band (see Tables 4 and 5).

As noted by Willett et al. (2011b), most OHMGs occupy the upper branch, only a handful being found along the lower branch (defined by a wide range of PAH EW but relatively weak silicate absorption), which is where most non-OHMG ULIRGs and optically identified AGNs are also found.

IRAS16399N is located in the upper branch, among the OHMGs, and consistent with a strong obscuration of the nuclear source. However, the nature of the nuclear source is unclear from the "fork diagram." On the other hand, IRAS16399S is located near the "knee" (high PAH EW, but low silicate absorption strength), where the OHMG and non-OHMG samples overlap. This is also where starburst galaxies tend to be found (Spoon et al. 2007).

3.2.2. Mid-IR Photometry

The flux in 8 μm *Spitzer* passband is normally attributed to PAH molecules (Leger & Puget 1984; Allamandola et al. 1985; Puget & Leger 1989), which are heated by single UV and optical photons in the interstellar radiation field (ISRF) of galaxies or near B stars (e.g., Li & Draine 2002; Haas et al. 2002; Peeters et al. 2004; Wu et al. 2005). The 8 μm emission has been used as an indicator of photodissociation regions (PDRs) associated with H II regions (Helou et al. 2004; Wu et al. 2005) and correlates very well with optical and radio tracers of ionizing photons (Wu et al. 2005; Calzetti et al. 2005). As can be seen in Figure 1, the 8 μm image of IRAS16399−0937 shows both nuclei as compact sources embedded in an extended envelope. The two nuclei are linked by a ridge of emission that crosses the dust lane complex that is prominent at optical wavelengths. Spurs extend to the west and from the IRAS16399N nucleus to the northeast, the latter corresponding to the northeastern blob observed in shorter-wavelength images. The 8 μm emission arising between and to the east of the nuclei is brightest within the region bounded (at shorter wavelengths) by the IRAS16399S nucleus and the western arc; it is presumably due to dust heated by embedded star formation.

While the 24 μm emission is known to be dominated by interstellar dust, there is an increasing contribution from stellar photospheric emission at shorter wavelengths. In the IRAC channels, stellar emission dominates at 3.6 μm, whereas the strong 7.7 μm PAH feature falls into the 8.0 μm channel, which therefore predominantly maps ISM emission. The stellar contribution to the 8 μm channel can be approximately removed by extrapolating the 3.6 μm emission, following the prescription of Helou et al. (2000),

$$F_{(8\mu\mathrm{m,dust})} = F_{(8\,\mu\mathrm{m})} - 0.232 F_{(3.6\,\mu\mathrm{m})}. \quad (2)$$

Isophotes of the resulting ISM PAH-dust 8 μm emission are plotted in Figure 2, which also shows the continuum-subtracted Hα + [N II] emission and the 1.49 GHz radio image.

We estimated SFRs from the ISM PAH-dust 8 μm emission, using the relation given by Wu et al. (2005),

$$\mathrm{SFR}_{(8\,\mu\mathrm{m,dust})} = \frac{\nu\, L_\nu(8\,\mu\mathrm{m,\ dust})}{1.39 \times 10^9\, L_\odot}\,(M_\odot\ \mathrm{yr}^{-1}). \quad (3)$$

The measured values of $F_{(8\,\mu\mathrm{m,dust})}$ and estimated $\mathrm{SFR}_{(8\,\mu\mathrm{m,dust})}$ for the whole IRAS16399−0937 system (using the flux measured within an aperture of radius 7.″0) and both the IRAS16399N and IRAS16399S nuclei (using apertures of radius 2.″02) are given in Tables 1 and 3, respectively.

The continuum emission in the MIPS 24 μm band can be attributed to very small grains with effective radii in the 15–40 Å range. Such grains efficiently convert stellar UV (~6–13.6 eV) photons into ~24 μm continuum emission (see Li & Draine 2001; Draine et al. 2007) and thus, 24 μm emission is considered to be a good tracer of star formation (Calzetti et al. 2005; Draine & Li 2001; Draine 2003). On the other hand, 24 μm emission can also arise due to thermal emission from large dust grains heated by AGNs (Bendo et al. 2006a, 2006b; Smith et al. 2007). Although the double nucleus of IRAS16399−0937 is unresolved in the MIPS 24 μm image, Haan et al. (2011) inferred that the N component contributes ≈90% of the 24 μm flux, suggesting that the AGN may be dominating the excitation of small dust grains, in agreement with results obtained by Brandl et al. (2006), who claim that if the galaxy hosts an AGN, the dust heated by the AGN might dominate the continuum emission at 24 μm (Brandl et al. 2006; Diamond-Stanic & Rieke 2010).

Nevertheless, if we assume that the 24 μm emission is due to star formation rather than AGN heating, the SFR can be estimated from the correlation proposed by Rieke et al. (2009),

$$\mathrm{SFR}_{24\,\mu\mathrm{m}} = 7.8 \times 10^{-10}\, \nu\, L_\nu(24\,\mu\mathrm{m}, L_\odot) \times [7.76 \times 10^{-11}\, \nu\, L_\nu(24\,\mu\mathrm{m}, L_\odot)]^{0.048} (M_\odot\ \mathrm{yr}^{-1}). \quad (4)$$

Measuring the 24 μm flux in a circular aperture of radius 7″ (see Table 1), we find an SFR of 23.18 $M_\odot$ yr^{-1} (Table 3).

While their similar *H*-band luminosities suggest that the two nuclei also have similar stellar masses, the IRAS16399N nucleus is the dominant source of mid-IR dust emission. As can be seen in Figure 2, this is also the case for PAH emission: the dominant peak is associated with the IRAS16399N nucleus, with a spur approximately coincident with the NE plume. The weaker PAH emission peak associated with the IRAS16399S nucleus is offset relative to the H II regions, which border it to the south. PAH emission also extends north-west and appears to be associated with the complex of dust lanes bounded by the western arc connecting the IRAS16399S nucleus to the NE plume.

3.3. Radio Source

The radio source at 1.49 GHz exhibits a morphology very similar to that of the 8μm PAH-dust emission, with a bright core associated with the IRAS16399N nucleus, which is elongated to the NE, a secondary peak associated with the IRAS16399S nucleus that coincides with the PAH emission peak and a knotty extension to the NW overlapping the dust lane complex (Figures 1 and 2). This striking morphological similarity strongly suggests that the extended radio emission is due to star formation, rather than an AGN jet.

Similarly, Baan & Klöckner (2006) classified the nuclear radio source as starburst-dominated based on consideration of three criteria: spectral index, brightness temperature and the FIR–radio luminosity ratio (q).

The spectral index map (Figure 7) shows that the bright, compact core component associated with the IRAS16399N nucleus has a steep spectrum, $\alpha = -0.75 \pm 0.08$, consistent with optically thin synchrotron radiation and characteristic of normal spirals, extended starbursts and compact starbursts in ULIRGs (Gioia et al. 1982; Condon 1983; Condon et al. 1991). However, steep spectrum radio cores are also commonly observed in Seyfert galaxies (e.g., Sadler et al. 1995; Roy et al. 2000; Kharb et al. 2010), so this does not necessarily preclude a significant AGN contribution.

We estimated the brightness temperature, (T_B), of the core component using the relation,

$$T_B = 1.8 \times 10^9 (1+z) \left(\frac{S_\nu}{1\,\mathrm{mJy}}\right) \left(\frac{\nu}{1\,\mathrm{GHz}}\right)^{-2} \left(\frac{\theta_1\theta_2}{\mathrm{mas}^2}\right)^{-1} \mathrm{K}, \quad (5)$$

where z is the redshift, θ_1 and θ_2 are the major and minor axes of the source (e.g., Ulvestad et al. 2005). For a "deconvolved" core of size = 1.″1 × 0.″5, and an integrated flux density = 15.3 mJy as derived from the AIPS task JMFIT, $T_B \sim 2.3 \times 10^4$ K at 1.49 GHz. For the southern nucleus, $T_B \sim 878$ K, for an integrated flux density of 6.8 mJy and a "deconvolved" core size of 2.″9 × 2.″2. At 1.49 GHz, the maximum brightness temperature for supernovae synchrotron emission in a starburst

is $T_B < 10^5$ K (see Condon et al. 1991, Equation (8)), which is consistent with the value derived for the IRAS16399S nucleus. In contrast, radio core sources in Seyferts, even those exhibiting steep spectra, typically have brightness temperatures in the range $10^5 \lesssim T_B \lesssim 10^7$ K (Kukula et al. 1999; Giroletti & Panessa 2009). However, we note that in nearby Seyferts, high brightness temperatures ($T_B \gtrsim 10^5$ K) are observed only in radio knots and cores; the extended radio emission typically having a much lower brightness temperature. At the distance of IRAS16399−0937, the high and low brightness temperature regions would be unresolved within the core, leading to a measured brightness temperature below the range quoted above. Therefore, while the brightness temperature of the core radio component is therefore consistent with star formation, we cannot exclude the possibility of an AGN contribution

The third criterion used by Baan & Klöckner is based on the well-established correlation between the FIR and radio luminosities; for a given FIR luminosity, galaxies hosting AGN radio sources are expected to have a higher radio luminosity than pure starbursts and hence a lower value of q (e.g., Condon et al. 1991; Yun et al. 2001). Baan & Klöckner found that $q \approx 3$ for IRAS16399−0937, placing it firmly in the starburst regime. However, whereas the radio core has a size $\sim 1''$, the *IRAS* FIR fluxes used to determine q are characteristic of the entire $\sim 15''$ system (including both nuclei and the envelope), which is unresolved in *IRAS* data. It is not clear what fraction of the FIR luminosity arises from the IRAS16399N nucleus alone, but it is evident from the Hα + [N II] and the ISM PAH-dust 8 μm images that star formation is widespread throughout the system, with the IRAS16399N nucleus contributing, for example, only ≈20% of the ISM PAH-dust 8 μm emission (Table 1). The values of q estimated by Baan & Klöckner should therefore be regarded as a high upper limit for the radio core in the IRAS16399N nucleus.

Unfortunately, as the IRAS16399N nucleus cannot be isolated in MIPS images, it is not possible to determine a more representative value of q using *Spitzer* data.

In summary, therefore, the clearest clue to the origin of the compact radio core associated with the IRAS16399N nucleus is provided by the brightness temperature, which suggests that it is dominated by a compact starburst rather than a radio-bright AGN.

Assuming that the 1.49 GHz radio emission is entirely due to star formation activity, we estimate SFRs for the IRAS16399N and IRAS16399S nuclei using Equation (27) of Condon et al. (2002)

$$\mathrm{SFR}_{1.49\,\mathrm{GHz}}(M_\odot\ \mathrm{yr}^{-1}) \approx \frac{L_{1.49\mathrm{GHz}}(\mathrm{W\,Hz}^{-1})}{4.6 \times 10^{21}}. \quad (6)$$

These turn out to be $\mathrm{SFR}_{1.49\,\mathrm{GHz}} = 6.04\ M_\odot\ \mathrm{yr}^{-1}$ for the IRAS16399N nucleus and $\mathrm{SFR}_{1.49\,\mathrm{GHz}} = 2.68\ M_\odot\ \mathrm{yr}^{-1}$ for the IRAS16399S nucleus, respectively (Table 3).

3.4. X-Ray Source

The peak of the compact (unresolved) X-ray source is clearly associated with IRAS16399N (Figure 8). However, there are also fainter knots of X-ray emission located approximately 4″ to the N and NE of IRAS16399N, which border the radio source and appear to be associated with the amorphous region of *B*-band and Hα+[N II] emission. Yet fainter blobs of X-ray emission are associated with IRAS16399S and extend along the western arc.

The luminosity of the compact source associated with IRAS16399N is $\sim 4.69 \times 10^{40}$ erg s^{-1}, much lower than is typical for Seyfert 1 nuclei (which have $42 \lesssim \log L_{2-10\,\mathrm{keV}} \lesssim 44$; e.g., Georgantopoulos & Akylas 2010; Jin et al. 2012) but comparable with nearby low luminosity AGNs (Ho 2009).

Ranalli et al. (2003) argue that star formation accounts for the most of the hard X-ray emission of low luminous AGNs. Based on X-ray and IR data of a sample of local star-forming galaxies, these authors derived an empirical relation between SFR and X-ray luminosity emission,

$$\mathrm{SFR}^{0.5-2\,\mathrm{keV}}_{\mathrm{X-ray}}\,(M_\odot\ \mathrm{yr}^{-1}) = 2.2 \times 10^{-40} L^{0.5-2\,\mathrm{keV}}_{\mathrm{X-ray}}. \quad (7)$$

Assuming that the X-ray emission from IRAS16399−0937 is produced entirely by star formation, we find $\mathrm{SFR}^{0.5-2\,\mathrm{keV}}_{\mathrm{X-ray}} = 10.32\ M_\odot\ \mathrm{yr}^{-1}$ for the IRAS16399N nucleus and $\mathrm{SFR}^{0.5-2\,\mathrm{keV}}_{\mathrm{X-ray}} = 2.46\ M_\odot\ \mathrm{yr}^{-1}$ for the IRAS16399S nucleus, respectively (Table 3).

4. SPECTRAL ENERGY DISTRIBUTION MODELING

The flux density measurements summarized in Table 1 were combined with the extracted IRS SL and LL spectrum to construct SEDs for the IRAS16399−0937 system as well as both nuclei. Flux densities obtained from 7″ (or 36″ in the case of the *Herschel* data) apertures were used to form the 0.4–500 μm SED for the system as a whole. SEDs covering the range 0.4–14 μm were also constructed for each nucleus, using measurements from 2″ apertures and the corresponding extractions from the IRS SL spectrum. The SEDs of both nuclei were simultaneously fit as described below using a new Markov Chain Monte Carlo code. The nuclei are not resolved in the IRS LL spectrum, or in the MIPS or *Herschel* data, i.e., for wavelengths >14 μm. These data were included in the SED fits but treated as upper limits (see the Appendix for details).

4.1. SED Model Components

We decomposed the infrared spectra and SEDs using a customized version of our code clumpyDREAM (J. Gallimore, in preparation). clumpyDREAM makes the usual assumption that the infrared SEDs of galaxies can be decomposed into a sum of contributions from stars (photospheric emission), interstellar dust and PAHs (the ISM component), and reradiation from the dusty torus surrounding an AGN (Walcher et al. 2011; Genzel & Cesarsky 2000). The code also allows for contributions from very hot (∼1500 K), presumably carbonaceous dust grains and AGN-heated dust in an NLR. However, the hot dust component is found only in QSOs and Type 1 AGNs, and the NLR contribution is required only to fit silicate emission profiles (see Mor et al. 2009). Since IRAS16399−0937 is neither type 1 nor shows silicate in emission, the hot dust and NLR components are not included in the SED fits.

We used GRASIL (Silva et al. 1998) models of elliptical galaxies to fit the stellar contribution. These models simulate a short (∼1 Gyr) burst of star formation followed by passive evolution, and the model grids span a range of metallicity and age of the stellar population. Since stars contribute significantly only to our near-infrared and optical broadband (<5.0 μm) measurements, there is insufficient information to constrain the metallicity of the stellar population. The metallicity of ULIRG nuclei varies, with some evidence for sub-solar oxygen abundance and super-solar neon abundance; on average, a typical ULIRG probably has slightly super-solar abundance

Table 6
Summary of Model Parameters used for SED Decomposition

Parameter	Description	Values
σ	Torus angular scale height (deg)	15, 20, 25, 30, 35, 40, 45, 50, 55, 60, 65, 70
Y	Torus radial extent	5, 10, 20, 30, 40, 50, 60, 70, 80, 90, 100
N_0	Torus number of clouds	1, 2, 3, 4, 5, 6, 7, 8, 9, 10, 11, 12, 13, 14, 15
q	Torus radial power law index	0.0, 0.5, 1.0, 1.5, 2.0, 2.5, 3.0
τ_V	Torus cloud optical depth	5, 10, 20, 30, 40, 60, 80, 100, 150
i	Torus inclination (degrees)	0, 10, 20, 30, 40, 50, 60, 70, 80, 90
$q_{\rm PAH}$	ISM PAH mass fraction	0.47, 1.12, 1.77, 2.5, 3.19, 3.9, 4.58
$u_{\rm min}$	ISM ISRF scaling	0.1, 0.15, 0.2, 0.3, 0.4, 0.5, 0.7, 0.8, 1.0, 1.2, 1.5, 2.0, 2.5, 3.0, 4.0, 5.0, 7.0, 8.0, 10.0, 12.0, 15.0, 20.0, 25.0
Age	Age of stellar population (Gyr)	0.1, 0.2, 0.4, 0.8, 1.5, 2.0, 3.0, 4.0, 5.0, 8.0, 11.0, 13.0

($Z \approx 1.1\,Z_\odot$; Clemens et al. 2008; Veilleux et al. 2009; Rupke et al. 2008). Therefore, we fixed the metallicity to solar, which should provide a reasonable approximation, but allowed the age of the stellar population to vary.

We used the models of Draine et al. (2007, hereafter DL07) to fit the ISM component. The primary strengths of the DL07 models are (1) they have been successfully employed to model the infrared SED of galaxies with a range of star-forming properties, including nearby quiescent and star-forming spiral galaxies (Draine & Li 2007), cold dust galaxies (Willmer et al. 2009), and more distant, luminous star-forming galaxies (Magdis et al. 2012); and (2) they permit a range of PAH feature strengths by tuning the PAH mass fraction. The models consist of a population of dust grains with common composition and size distribution from Weingartner & Draine (2001). The grains are heated by a scaled ISRF, $u_\nu = U u_{\nu,\rm solar}$, where u_ν is the energy density of the radiation field, U is a dimensionless scaling factor, and $u_{\nu,\rm solar}$ is the ISRF for the solar neighborhood (Mathis et al. 1983). Two heating environments are considered, (1) the diffuse ISM, in which grains are heated primarily by the diffuse ISRF, and (2) dust associated with star-forming regions, where the heating is dominated by direct starlight. The diffuse ISM is heated by a fixed energy density radiation field, $U = u_{\rm min}$, where $u_{\rm min}$ is a free parameter of the model. Star-forming regions are modeled by considering a power law distribution for U: $dM/dU \propto U^{-2}$ over the range $U = u_{\rm min}$ to $U = 10^6$, where M is the dust mass.

In the DL07 models, PAHs are modeled by adopting cross-sections (per C atom) and effective particle sizes chosen to mimic the emission observed in the nuclear regions of SINGS galaxies (Smith et al. 2007). The strength of the PAH spectral features relative to continuum is determined in part by the parameter $q_{\rm PAH}$, the fraction of the total dust mass that is in PAHs. In practice, average PAH compositions and ionization states will vary from galaxy to galaxy (Smith et al. 2007; Galliano et al. 2008), and so we expect a priori imperfect fits to the PAH features in detail for any particular galaxy SED. Nonetheless, examination of residual, misfit PAH features provides a means to compare individual galaxy PAH features to an effective SINGS mean PAH spectrum (Smith et al. 2007).

In sum, the spectral shapes of the ISM components are determined by two free parameters: $u_{\rm min}$ and $q_{\rm PAH}$. For simplicity and per the recommendations of DL07, we adopt the same values of $u_{\rm min}$ and $q_{\rm PAH}$ for both the diffuse ISM and star-forming regions. The diffuse ISM and star-forming regions are otherwise treated as separate spectral components for the purpose of determining the best fit. In the present analysis, different values of $u_{\rm min}$ and $q_{\rm PAH}$ were permitted for each nucleus of IRAS16399−0937. The relative fraction of the SFR component provides a measure of the dust luminosity that arises from SFRs; we use the prescription of DL07 (their Equation (29)) and calculate $f_{\rm PDR}$, the fraction of the dust luminosity that comes from PDRs with $U > 100$.

The AGN torus component was fit using the clumpy torus models of Nenkova et al. (2008a, 2008b).[19] In these models, the AGN, represented by a broken power-law SED, illuminates a parsec-scale distribution of dusty clouds, which then re-radiate at infrared wavelengths. The number of obscuring clouds along a given sight-line is given by

$$N = N_0 \exp(-(90^\circ - i)^2/\sigma^2), \quad (8)$$

where i is the inclination of the observer view relative to the torus axis, σ is the angular scale height, and N_0 is the average number of clouds expected along the equatorial ray of the torus; note that the geometry is essentially a flared disk with a surface blurred by a Gaussian-like distribution of clouds. For simplicity, each cloud is assumed to have the same optical depth, parameterized by τ_V.

The radial extent of the torus is set by sublimation at the inner edge and the parameter $Y = r_{\rm out}/r_{\rm in}$. From Nenkova et al. (2008a), the sublimation radius was set to 0.4 pc $(L_{\rm AGN}/10^{45})^{1/2}$ erg s^{-1}, the radius where the adopted grain mixture and grain size distribution would survive. The radial distribution of clouds follows a power law,

$$N_C \propto (r/r_{\rm in})^q\,, \quad (9)$$

where N_C is the number of clouds per unit length, and the normalization is determined by Equation (8). Nenkova et al. (2008a, 2008b) show that the mass of hydrogen gas for a clumpy torus model is $M_{\rm torus} = m_H N_H \int N_C dV$, where N_H is the hydrogen column density through a single cloud. The column density N_H was converted from τ_V using the Bohlin et al. (1978) conversion factor for $R_V = 3.1$. Nenkova et al. give simple formulas for a sharp-edged distribution of clouds and integer values of q. Since we are instead using a Gaussian distribution of clouds and non-integer values of q, we instead calculate the hydrogen mass by numerical integration.

To summarize, the shape of the torus SED is determined by six parameters: $(\sigma, Y, N_0, q, \tau_V, i)$. The AGN luminosity determines the normalization (Table 6).

Finally, clumpyDREAM also allows for partially covering, intrinsic foreground extinction. For this purpose, we used the

[19] More information is available at https://www.clumpy.org/.

isothermal turbulent foreground dust screen model of Fischera & Dopita (2005). For simplicity, we used the $R_V = 3.1$ Milky Way extinction model, which provides reasonable fits to the silicate absorption profile and extinction of the stellar component. The extinction and covering fraction of the stellar, ISM, and AGN components are fitted independently, and the AGN covering fraction due to the foreground extinction is taken to be unity. We present detailed description of our applied methodology to fit the IRAS16399−0937 SED in the Appendix.

4.2. SED Modeling Results

The mid-IR continuum of AGNs (with the exception of blazars) is believed to be dominated by thermal dust emission from the torus, the dust grains being heated by absorption of UV–optical radiation emitted by the accretion disk. In merging systems like IRAS16399−0937, the AGN, if present, may have been recently triggered by inflows of molecular gas, leading to enhanced SMBH accretion rates. However, it is unclear how the formation of the dusty torus structure is related to the triggering of AGN activity. Perhaps the molecular gas inflows form the torus, which then acts as a fuel reservoir for the accretion disk. However, it has also been suggested that the torus is formed by a hydromagnetic accretion disk wind (Elitzur & Shlosman 2006), in which case the onset of AGN activity would precede torus formation. As already noted (Section 1), there is evidence in some objects that the OHMs are distributed in a disk-like structure that may be associated with the torus. There is no evidence that such a structure has formed in IRAS16399−0937, whose OHM have not been mapped at high spatial resolution. Nevertheless, for our purposes, the Nenkova et al. (2008a, 2008b) clumpy torus model is sufficiently general that it can represent a range of configurations for the distribution of AGN heated dust clouds, ranging from a thin disk to quasi-spherical.

The evidence that the IRAS16399N nucleus of IRAS16399−0937 contains an AGN is ambiguous. The optical spectrum is characteristic of LINERs, suggesting that it is a low luminosity AGN. On the other hand, IRAS16399−0937 lacks the high ionization mid-IR emission lines that are believed to be AGN signatures, while the properties of the compact radio source associated with the IRAS16399N nucleus are consistent with a stellar origin, rather than an AGN. Nevertheless, the steep rise in the mid-IR continuum suggests excess warm dust emission that is not present in the IRAS16399S nucleus.

clumpyDREAM was used to perform simultaneous fits to the SEDs of the IRAS16399N and IRAS16399S nuclei. Two sets of fits were run utilizing different models for the IRAS16399N nucleus in order to test for the presence of an AGN contribution. The two nuclei have to be fit simultaneously to accommodate data taken in large apertures that encompass both nuclei. We need to ensure during the fit that the sum of the model SEDs of the two nuclei does not exceed the upper limits in large apertures.

In the first set, the SED model for the IRAS16399N nucleus includes the clumpy torus component (that is, the AGN heated dust component) in addition to the stellar and ISM components. In the second, the torus component is turned off and only the latter two components contribute to the SED. The SED model for the IRAS16399S nucleus includes only the stellar and ISM components in both cases.

The results of the fits are illustrated in Figure 11 for the model that includes a torus contribution to the IRAS16399N nucleus and in Figure 12 for the model that excludes the torus component. In both figures, the fits to the IRAS16399N and IRAS16399S nuclei are shown in the upper and lower panels,

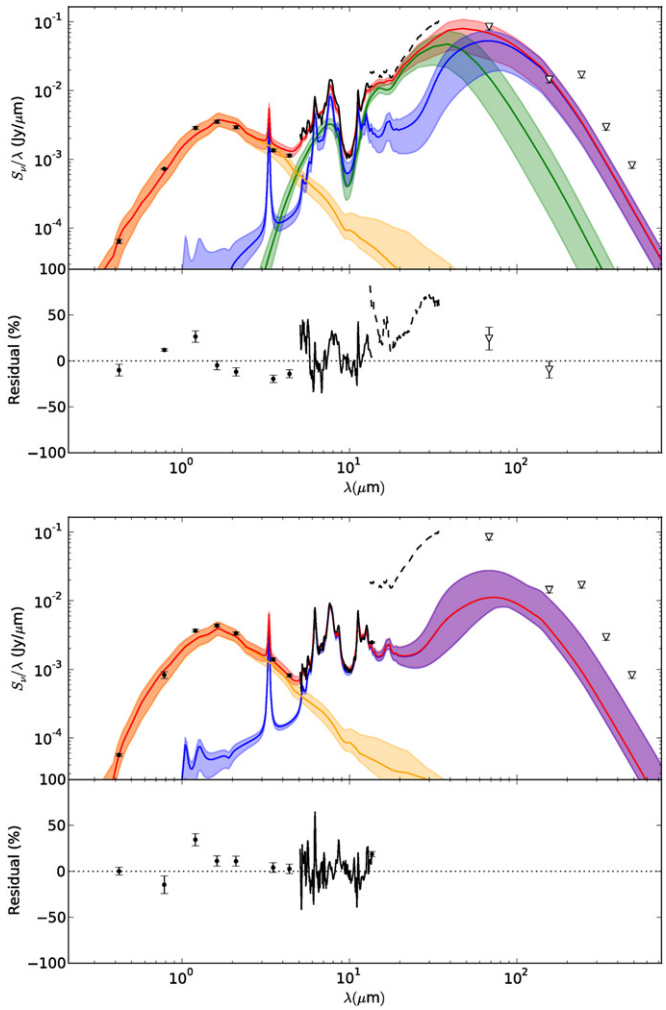

Figure 11. Fits to the 0.4–500 μm spectral energy distributions of the north (top) and south (bottom) nuclei of IRAS16399−0937. The symbols with error bars represent photometry from *HST*, 2MASS, *Spitzer*, and *Herschel* (see Table 1); the black lines represent IRS SL (solid) and IRS LL (dashed) spectra. The overall fit, shown by the red band, is the sum of three components: the GRASIL elliptical galaxy models (orange band, Silva et al. 1998), the ISM dust + PAH models of DL07 (blue band), and the clumpy AGN torus model of Nenkova et al. (2008a, 2008b; green band). The fits to both nuclei were carried out simultaneously using the clumpyDREAM code (see text). The width of each band represents, at a given wavelength, the full range of flux density permitted by the converged fit. In this model, it is assumed that the IRAS16399N nucleus contains an AGN, whereas the IRAS16399S nucleus is a pure starburst. Therefore, the fit to the IRAS16399N nucleus (top panel) includes all three components, whereas the fit to the IRAS16399S nucleus (bottom panel) includes only the stellar and ISM components. The two nuclei are not resolved in the LL IRS spectrum, or in the *Spitzer* MIPS and *Herschel* SPIRE images. Therefore the LL spectrum (dashed line) and photometry data points for $\lambda \geqslant 30\,\mu$m (inverted triangles) refer to large aperture (7″) measurements of IRAS16399−0937 system and were treated as upper limits in the fits.

respectively. As a consistency check, the sum of the fitted SED models (i.e., the sum of the fits to each nucleus) is compared to the SED of the IRAS16399−0937 system derived from large apertures (Table 1) for both sets of fits (Figure 13). The combined model SED does not exceed the observed system SED by more than ∼10%, comparable to the accuracy of the SED models and the absolute calibration accuracy for the far-infrared data points.

Estimators of the probability densities of the fitted parameters for both nuclei in both SED models are shown in Figures 14–18. The median, 5th and 95th percentile values of the parameters are listed in Tables 7 and 8, along with the derived SFRs.

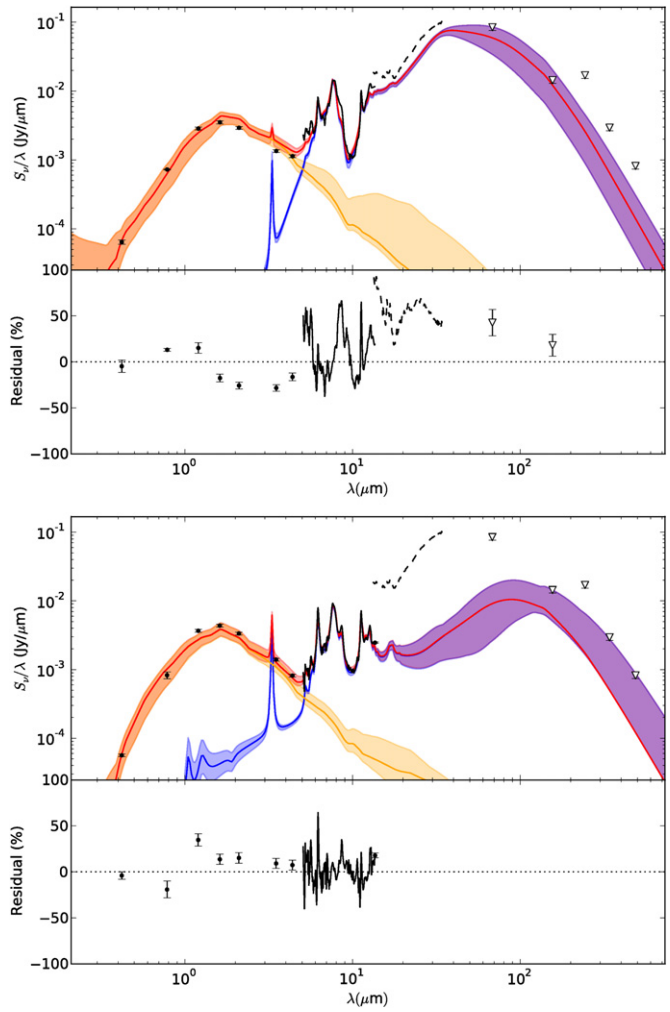

Figure 12. Same as Figure 11 for the case in which the SED fits to both the IRAS16399N (top) and IRAS16399S (bottom) nuclei include only stellar (orange band) and ISM (blue band) components.

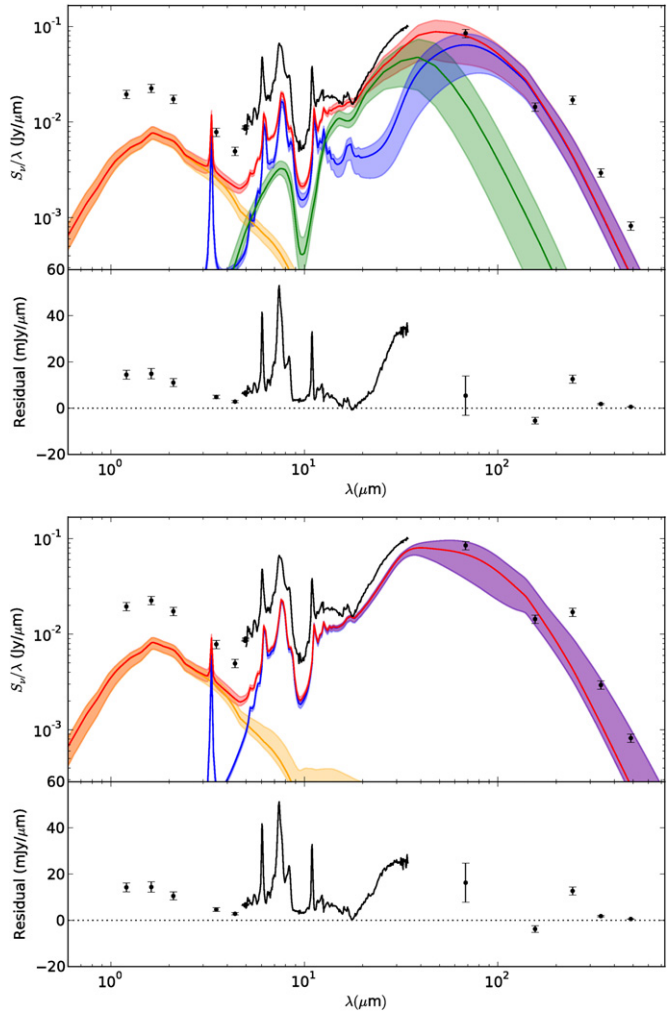

Figure 13. Comparison of the summed SED fits of Figures 11 (top) and 12 (bottom) to the SED of the IRAS16399−0937 system obtained from large aperture (7″) photometry (inverted triangles) and IRS SL and LL spectroscopy (dashed line). The summed small aperture (2.″02) fluxes of the IRAS16399N and IRAS16399S nuclei are also plotted for wavelengths $<14\mu$m, where the nuclei are resolved (filled points and solid line). The top panel shows the sum of the SED models fitted to the IRAS16399N and IRAS16399S nuclei, for the case in which an AGN torus is included in the fit to the IRAS16399N nucleus. The bottom panel shows the summed SED fit for the case in which both IRAS16399N and IRAS16399S nuclei were fitted using only stellar and ISM components. Note that the sum of the SED models does not exceed the upper limits imposed by the large aperture measurements.

4.2.1. AGNs and Starburst Nucleus

Here we summarize the results of the SED fit, which includes a clumpy torus contribution to the IRAS16399N nucleus. The fits to the IRAS16399N and IRAS16399S nuclei are shown in Figure 11. The probability density estimators for the fitted parameters are shown in Figure 14 and the parameter values given in Table 7. It can be seen that the observed SED of the IRAS16399N nucleus is well fit by the combination of the three components. The optical–NIR continuum below 3.5 μm is well fit by an evolved stellar population with an age of $\log \approx 12.6$ Gyr. The torus and ISM components are comparable in strength below $\approx$10 μm but the torus emission peaks around 40 μm and is the main contributor to the mid-to-far infrared continuum between 10 and 70 μm. The ISM components dominates at wavelengths $\gtrsim 70$ μm.

The strength of the torus component in the SED fit rather tightly constrains the bolometric luminosity of the AGN, $L_{\rm AGN} \approx 3.4 \times 10^{44}$ erg s^{-1}. However, although this implies that the IRAS16399N nucleus hosts a moderately luminous AGN (comparable with Type 1 Seyfert galaxies), the torus parameters derived from the fit indicate that it is deeply embedded within a quasi-spherical distribution of optically thick clouds. The torus has a large angular scale height, $\sigma \gtrsim 66°$, and is also radially extended, $Y \gtrsim 60$. The average number of clouds along an equatorial ray is $N_0 \gtrsim 14$. Note that the probability distributions for these parameters are truncated at the maximum values sampled by the model grid (Figure 14), and the recovered median values given in Table 7 may therefore be underestimates. Individual clouds have an optical depth of $20 \lesssim \tau_V \lesssim 35$ mag. The torus inclination to the line of sight is not well constrained, but is probably $i \gtrsim 60°$. Taking the median values of i, σ, and N_0, we estimate that there are $\sim$14 clouds along the observer's line of sight (Equation (8)). The line-of-sight escape probability for AGN photons is $\sim 10^{-6}$. Clearly, in this model, the AGN is very heavily obscured along the line of sight. However, the angular height of the torus is such that, even for a line of sight along the axis ($i = 0$), we predict $\approx$3 intervening clouds (corresponding to an escape probability $\sim$0.1). It should be noted that increasing N_0 and σ would likely not improve the fit, since the covering fraction is already unity. We could conclude that we have lower limits for N_0 and σ.

Considering the global energetics, the covering fraction due to the clumpy torus is $C_{\rm tor} \gtrsim 0.998$, implying that $\lesssim$0.2% of the AGN photons escape from the torus without being absorbed. This is consistent with the absence of signs of powerful AGN activity in the optical and *Spitzer* mid-IR spectrum (see Section 3.2.1). As already noted, the IRAS16399N nucleus has an optical spectrum characteristic of LINERs, which are generally regarded as low luminosity AGNs. The emission lines in LINERs are often attributed to photoionization by a weak AGN radiation field, although alternative models invoking shock ionization have also been advocated. Photon counting arguments show that the embedded AGN in IRAS16399−0937 cannot account for the observed line emission from IRAS16399N. Given the bolometric luminosity determined by the fit, integrating over the AGN spectrum adopted by Nenkova et al. (2008a, as defined by Equation (13)) for the clumpy torus model yields an ionizing photon luminosity $Q_{\rm AGN} \approx 3.6 \times 10^{54}$ photons s^{-1}. Taking the median value $C_{\rm tor} = 0.999$, the number escaping the torus is $Q_{\rm esc} = (1 - C_{\rm tor})Q_{\rm AGN} \approx 3.610^{53}$ photons s^{-1}. Assuming that the escaping photons are absorbed by photoionizing hydrogen in the surrounding ISM, the Hα luminosity resulting from recombination will be $L_{\rm H\alpha,pred} \approx C_{\rm ISM} p_{\rm H\alpha} h\nu_{\rm H\alpha} Q_{\rm esc}$, where $C_{\rm ISM}$ is the covering fraction of the surrounding gas and $p_{\rm H\alpha} \approx 0.45$, is the fraction of H$\alpha$ photons emitted per H recombination (assuming an electron density $n_e = 10^2$ cm^{-3} and temperature $T_e = 10^4$ K). If $C_{\rm ISM} = 1$, $L_{\rm H\alpha,pred} \approx 4.9\times10^{39}$ erg s^{-1}, which is $\lesssim$2% of the measured luminosity for IRAS16399N ($L_{\rm H\alpha} \approx 3.27 \times 10^{41}$ erg s^{-1}; Section 3.1). Thus, even if all the escaping AGN photons are absorbed by the gas ($C_{\rm ISM} = 1$), the attenuated AGN radiation field cannot account for the observed Hα luminosity. This implies that the LINER spectrum cannot result from photoionization of the surrounding ISM by the embedded AGN.

The properties of the ISM component of the IRAS16399N nucleus are also constrained by the SED fit. In particular, the inferred ISM luminosity is $L_{\rm ISM} \approx 3 \times 10^{44}$ erg s^{-1}, implying an SFR of $\sim$12 $M_\odot$ yr^{-1}. The torus (by definition), stellar, and ISM components are all essentially completely covered by foreground extinction of varying optical depth ($\tau_V \approx 9$, 4.5, and 7 mag, respectively), suggesting that the IRAS16399N nucleus is submerged in a gas- and dust-rich environment.

As IRAS16399S was spectroscopically classified as a starburst (Baan et al. 1998), only the stellar and ISM components were included in the SED fit. The SED is well reproduced with this combination (Figure 12). The luminosity of the ISM component in IRAS16399S is a factor of ≈3 smaller than that of IRAS16399N, $L_{\rm ISM} \approx 9 \times 10^{43}$ erg s^{-1}, corresponding to an SFR $\sim$3.6 $M_\odot$ yr^{-1}. The fit also suggests that the IRAS16399S nucleus has a somewhat younger stellar population, with an age of log 10 Gyr, and the fraction of the dust luminosity coming from PDRs ($U > 100$), $f_{\rm PDR}$, is a factor of $\sim$17 larger than in the IRAS16399N nucleus, perhaps also indicating a younger stellar population than that of IRAS16399N.

In summary, the results of the SED-fitting suggest that IRAS16399N nucleus contains an embedded AGN but also hosts a star forming region which has luminosity and SFR roughly three times that of the IRAS16399S "starburst" nucleus.

4.2.2. Dual Starburst Nuclei

In order to test the alternative scenario in which the IRAS16399N nucleus does not contain an AGN, we also fitted the SEDs using only stellar and ISM components for both nuclei. Not surprisingly, the fit to the IRAS16399S nucleus is almost indistinguishable from that obtained in the previous case and very similar parameter values are recovered for the ISM component (Figure 12, Table 8). In particular, there is no significant difference in the luminosity of the ISM component and hence the SFR.

The overall fit to the IRAS16399N nucleus SED using only the stellar and ISM components is qualitatively similar to that obtained with the torus component (Figure 11), although, formally, this solution is not as good according to the Bayes information criterion (BIC) statistic,[20] which has values of 987 and 1225 for the models with and without the torus, respectively.

In order to compensate for the absence of the torus contribution to the mid-IR, the fraction of the ISM luminosity coming from PDR dust increases radically, from $f_{\rm PDR} < 1.4\%$ to ≈70%. Removing the torus effectively creates a gap in the mid-infrared, and the no torus model compensates by requiring a greater contribution from the hot dust associated with PDRs.

The PAH mass fraction in the IRAS16399N nucleus ($q_{\rm PAH} \approx 0.5$) is a factor of $\sim$3 smaller in the absence of the torus component and is therefore also an order magnitude smaller than that in the IRAS16399S nucleus (which is similar in the two models). This is a consequence of the fact that when the torus is included, the relatively low observed EW of the PAH features results from dilution by the torus hot dust continuum. When the torus is omitted, the PAH EWs are matched mainly by decreasing $q_{\rm PAH}$. It is also notable that the foreground extinction to the ISM component is greatly increased in the fit without the torus component, $\tau_{{\rm ISM},V} \approx 24$, compared to ≈6.9 with the torus. This is mainly driven by the strength of the 9.7 μm silicate absorption feature. When the torus is present, this feature is produced by combination of torus and ISM extinction. Without the torus, the silicate absorption is produced exclusively by foreground extinction due to the ISM component, resulting in an increased $\tau_{{\rm ISM},V}$.

As the "no torus" model requires a much stronger ISM component, it also implies a higher SFR for the IRAS16399N nucleus, since star forming regions are the main heating source for the ISM. Thus, we obtain an SFR $\sim$ 20 $M_\odot$ yr^{-1}, nearly a factor of two greater than derived for the model including the AGN torus (see Tables 7 and 8).

5. DISCUSSION

Our multiwavelength study of IRAS16399−0937 combines new *HST* ACS *I*-band and emission line images with archival *Spitzer* IRAC, IRS, and MIPS data, *Herschel* photometry, and VLA images at 1.49 and 4.9 GHz. These data provide a comprehensive picture of the overall morphology of this system and the spatial distribution of the ionized gas, dust and radio emission. We have also compiled a broad-band SED for the system, spanning 0.45–500 μm, which, importantly, resolves the two nuclei at wavelengths below 14 μm.

5.1. IRAS16399−0937 as an Individual Object

According to Haan et al. (2011)'s study of the nuclear structures in nearby LIRGs, merging systems can be classified into six different merger stages: (1) separate galaxies, but disks symmetric (intact) and no tidal tails, (2) progenitor galaxies distinguishable with disks asymmetric or amorphous and/or tidal tails, (3) two nuclei in common envelope, (4) double nuclei

[20] The BIC is $-2 \cdot \ln\hat{L} + k \cdot \ln(n)$, which is estimated by $\chi^2 + k \cdot \ln(n)$, where $\hat{L}$ is the maximized value of the likelihood function of the model, k is the number of free parameters and n is the number of data points. The smaller BIC value indicates the preferred model (Schwartz 1978).

Table 7
Parameters Derived from SED Fits Assuming AGNs and Starburst Nuclei

Parameters	IRAS16399N			IRAS16399S		
	Median	5%	95%	Median	5%	95%
			Clumpy torus model			
σ	69.°0	65.°8	69.°9	...	...	...
Y	90.1	63.4	99.2	...	...	...
N_0	14.7	13.9	15.0	...	...	...
q	0.92	0.59	1.00	...	...	...
τ_V	27.7	20.6	34.8	...	...	...
i	75.°8	57.°9	88.°5	...	...	...
$C_{\rm frac}$	99.9%	99.8%	99.9%	...	...	...
escProb		$\leqslant 1 \times 10^{-6}$		...	...	...
Mass ($M_\odot$)	347	174	589	...	...	...
Size (pc)	20.9	13.5	24.5	...	...	...
			Interstellar medium			
$u_{\rm min}$	22.8	14.7	24.9	15.9	6.9	23.3
$q_{\rm PAH}$	1.41	1.07	2.16	4.01	2.93	4.51
$f_{\rm PDR}$	0.3%	0.0%	1.4%	5.1%	0.5%	13.0%
			Interstellar medium foreground			
$\tau_{{\rm ISM},V}$ (mag)	6.9	4.5	10.1	14.1	1.9	48.73
$C_{\rm frac,ISM}$	89.1%	62.8%	99.2%	23.8%	7.6%	79.7%
$\tau_{{\rm torus},V}$ (mag)	9.0	5.5	12.0	...	...	...
$\tau_{{\rm stars},V}$ (mag)	4.5	4.0	5.0	3.4	3.1	3.7
$C_{\rm frac,stars}$	98.7%	98.3%	99.1%	99.6%	99.0%	100%
			Simple stellar population			
log age (Gyr)	12.6	7.9	13.0	9.4	4.3	12.6
			Amplitude			
$L_{\rm AGN}$ (erg s^{-1})	3.4×10^{44}	2.7×10^{44}	4.2×10^{44}	...	...	...
$L_{\rm ISM}$ (erg s^{-1})	2.9×10^{44}	1.9×10^{44}	3.7×10^{44}	8.9×10^{43}	7.8×10^{43}	1.3×10^{44}
SFR ($M_\odot$ yr^{-1})	11.6	7.6	15.1	3.6	3.2	5.2

Notes. It should be noted the N_0, Y and σ have ran to the limits of the parameter grid of the clumpy model, consequently, there is no automatic detection of upper limits. See marginalized posterior probability densities in Figure 14.

Table 8
Parameters Derived from SED Fits Assuming dual Starburst Nuclei

Parameters	IRAS16399N			IRAS16399S		
	Median	5%	95%	Median	5%	95%
			Interstellar Medium			
$u_{\rm min}$	18.5	8.2	24.6	1.6	0.4	4.6
$q_{\rm PAH}$	0.48	0.47	0.52	4.31	3.66	4.56
$f_{\rm PDR}$	70.2%	60.0%	78.4%	10.9%	3.5%	18.9%
			Interstellar medium foreground			
$\tau_{{\rm ISM},V}$ (mag)	24.0	23.4	24.8	7.7	2.2	38.0
$C_{\rm frac,ISM}$	99.9%	99.5%	100%	34.9%	14.6%	89.1%
$\tau_{{\rm stars},V}$ (mag)	5.5	5.0	6.0	3.3	3.1	3.7
$C_{\rm frac,stars}$	98.8%	98.6%	99.9%	99.6%	99%	100%
			Simple stellar population			
log age (Gyr)	12.8	0.9	13.0	9.7	4.5	12.7
			Amplitude			
$L_{\rm ISM}$ (erg s^{-1})	5.06×10^{44}	4.50×10^{44}	5.83×10^{44}	8.18×10^{43}	7.46×10^{43}	9.93×10^{43}
SFR ($M_\odot$ yr^{-1})	20.32	18.11	23.44	3.32	3.04	4.02

plus tidal tail, (5) single or obscured nucleus with disturbed central morphology and short faint tails, (6) single or obscured nucleus with disturbed central morphology and short faint tails. Using their scheme IRAS16399−0937 is classified as type 3 (nuclei in common envelope) and this group constitutes 21.6% of a sample of 60 systems. However, the majority of their sample is classified as type 2 (25%), while 5 (8.3%) systems are classified as type 1, 8 (13.3%) are type 4, 12 (20%) are type 5, 1 (1.6%) is type 6, and 6 (10%) are classified as undisturbed isolated galaxies.

Rigopoulou et al. (1999) classified the ULIRG mergers as follows: (1) fully relaxed systems, in which we see only a single pointlike nucleus with relatively little or no tail; (2) systems in which the merger is completed; in such systems we see a single nucleus, but with significant residual structure or tail formation; and (3) interacting pairs in which the interacting nuclei are clearly visible and can be found in a variety of separations. Of 27 targets they studied, 68% appear to have double nuclei (similar to IRAS16399−0937), with a wide range of projected separations between the nuclear components.

In terms of separation, IRAS16399−0937 is at the lower end of the distribution for objects that have resolved double nuclei and also has a relatively low infrared luminosity ($L_{\rm IR} = 11.63\,L_{\odot}$; see Table 1 of Haan et al. 2011) compared with other (U)LIRGs (see Figure 11 of Rigopoulou et al. 1999). In Haan et al. (2011)'s sample, IRAS16399−0937 is slightly below the median projected separation (7.2 kpc; see Section 3.1 and Figure 4 of Haan et al. 2011) and the bulge luminosity derived from the *H*-band image is significantly lower than that of the majority of the (U)LIRGs studied in this sample. These studies lead us conclude that IRAS16399−0937 is not unusual in terms of its merger stage among (U)LIRGs and it also fits in with Haan et al. (2011)'s finding that non-merging LIRGs have larger bulge masses than merging LIRGs (see Figure 8 of Haan et al. 2011).

According to Yuan et al. (2010), IRAS16399−0937 is classified as a "close binary" (i.e., early stage merger) and systems turn out to be about 12% of the Southern Warm Infrared Galaxy sample (hereafter SWIG; Kewley et al. 2001), but about 30% of the merging/pair systems. The infrared luminosity of IRAS16399−0937 is very close to the mean for the combined LIRG sample selected from SWIG and the *IRAS* Bright Galaxy Survey (Veilleux et al. 1999). However, it is somewhat unusual in terms of its spectroscopic properties since the majority of the "close binary" LIRG systems exhibit H II or composite spectra while IRAS16399−0937 has a LINER+starburst double nucleus (see Figure 12 of Yuan et al. 2010).

As noted in Section 5.5, Yuan et al. (2010) also argue that there are few "genuine" LINERs among (U)LIRGs. They reclassify most previously identified LINERs as composite nuclei and note that the few (nine) remaining objects falling in the LINER region of the diagnostic diagrams are close to the Seyfert/LINER borderline (this includes IRAS16399−0937), or in the few remaining cases (particularly, the well-studied NGC 6240 and Arp220) are either starburst superwinds or shocks driven by galaxy collisions, rather than being low accretion rate AGNs (see Figure 15 and Section 4.1 of Yuan et al. 2010).

Our picture for IRAS16399−0937 is very similar to what is proposed for the double nucleus NGC 6240 (LIRG) and Arp220 (ULIRG) galaxies, except that they both have higher infrared luminosities and smaller separations (∼0.7 kpc for NGC 6240 and ∼0.3 kpc for Arp220). In general, IRAS16399−0937 is a fairly typical example of an LIRG merger, but one in which the AGN is deeply embedded, with the LINER spectrum arising through shocks rather than AGN photoionization.

5.2. Star Formation

The ISM-dust 8.0 μm PAH, mid-IR (24 μm) and radio luminosities indicate an SFR ∼20 $M_{\odot}\,{\rm yr}^{-1}$ for the entire system. The SFR derived from the X-ray luminosity is higher, nearly 50 $M_{\odot}\,{\rm yr}^{-1}$, but this is subject to large uncertainties. Nevertheless, in all wavebands in which the nuclei are resolved, the system SFR is notably larger than the sum of the rates derived for the two nuclei, which account for ∼30%–60% of the total SFR, depending on the waveband. Evidently, star formation activity is not especially localized to the nuclei, The X-ray, PAH, and radio luminosities all imply a higher SFR for IRAS16399N than for IRAS16399S. For IRAS16399S, the SFRs derived from those three bands are all consistent with a rate of ≈3 $M_{\odot}\,{\rm yr}^{-1}$. There is a much larger spread for IRAS16399N, with the X-ray and radio luminosities indicating higher rates (≈6–10 $M_{\odot}\,{\rm yr}^{-1}$) than the PAH luminosity (≈4 $M_{\odot}\,{\rm yr}^{-1}$, but it is possible that the AGN contributes to the X-ray and radio emission.

The SFRs derived from the Hα emission are approximately a factor of three smaller than those derived from the radio and mid-IR emission for both nuclei. The Hα SFR for the system is uncertain by at least a factor of three, since the extinction is poorly constrained. The upper limit on $\rm SFR_{H\alpha}$ (determined using the reddening of the IRAS16399S nucleus) approaches the values obtained for longer wavelengths. Nevertheless, morphological evidence suggests that even outside the nuclei, most of the current star formation occurring in IRAS16399−0937 is heavily obscured by dust—for example, the radio and PAH images indicate that star formation is occurring in the dust lane complex between and to the east of the nuclei, a region that is devoid of Hα+[N II] emission.

5.3. Does IRAS16399−0937 Host an AGN?

Classifications of nuclear activity in OHMG based on optical spectroscopy (Darling & Giovanelli 2006; Baan et al. 1998) imply a much higher incidence of AGNs than results from radio, mid-IR, and X-ray data (Baan & Klöckner 2006; Vignali et al. 2005). In the case of IRAS16399−0937, Baan et al. (1998) used emission line diagnostic diagrams pioneered by Baldwin et al. (1981) and extended by Veilleux & Osterbrock (1987, hereafter referred to as VO diagrams) to classify the IRAS16399N nucleus as a LINER and the IRAS16399S nucleus as a starburst, respectively. Yuan et al. (2010) arrived at essentially the same conclusion, using measurements of the emission line ratios from Kewley et al. (2001) and the refined classification scheme developed by Kewley et al. (2006).[21] Insofar as LINERs can be considered low luminosity and/or low accretion rate AGNs (for a review, see Ho 2008), the optical spectra appear to clearly indicate the presence of a weak AGN in the IRAS16399N nucleus. In other wavebands, however, the evidence is ambiguous. The IRAS16399N and IRAS16399S nuclei fall within the regions occupied by Seyferts and starbursts, respectively, in the PAH 6.2 μm/7.7 μm × 11.3 μm/7.7 μm diagram (Figure 9), although LINERs are mixed with starburst and H II galaxies in this diagram (Sales et al. 2010). On the other hand, the mid-IR spectrum lacks the high ionization fine structure lines, [Ne V] 14.3 μm (IP 97.1 eV) and [O IV] 25.8 μm (IP 55 eV), that are generally considered to be unambiguous tracers of AGN activity (e.g., Willett et al. 2011a). However, these lines fall into the wavelength band covered by LL module of IRS, which does not resolve the two nuclei, so the AGN line emission may be swamped by dust emission from the nuclei and envelope. It is also worth noting that such lines are not always detected in the nuclei of Seyfert 2 galaxies (Sales et al. 2010; Gallimore et al. 2010). There is both a compact radio source and a compact X-ray source associated with IRAS16399N. However, the radio

[21] The adopted classification for the IRAS16399S nucleus listed in Table 3 of Yuan et al. (2010) is "cp, composite," that is, a mixture of starburst and AGN spectra. However, IRAS16399S falls well within the starburst regions of two of the three diagnostic diagrams ([O III]/Hβ versus [S II]/Hα and [O III]/Hβ versus [O I]/Hα) and lies near the H II region—composite boundary in the remaining diagram ([O III]/Hβ versus [N II]/Hα).

source has a low brightness temperature that seems more consistent with star formation than with an AGN radio jet, while the *observed* X-ray luminosity is a factor of $\sim 10^{2-3}$ lower than expected for a typical Seyfert galaxy and could also be due to star formation. Nevertheless, we cannot rule out an AGN contribution in either band.

The results of the SED decomposition indicate that a moderate luminosity AGN ($L_{\rm bol} \sim 3.4 \times 10^{44}$ erg s^{-1}) is indeed present in the IRAS16399N nucleus. An AGN-heated clumpy torus is required, in particular, to account for excess mid-IR emission (as compared to the IRAS16399S nucleus) that is apparent as a steep rise in the SED for $\lambda > 10\,\mu$m. The SED fit obtained for IRAS16399N when the AGN torus component is significantly better than that obtained when the torus is omitted. However, there are also other reasons for favoring the torus model. If the torus is omitted, the ISM component must increase in strength to compensate, implying an SFR $\sim 20\,M_\odot$ yr^{-1}, which is significantly higher (by factors $\approx$2–5) than the SFRs inferred from the observations (Table 3). On the other hand, for the model including the torus, the derived SFR agrees with that derived from the X-ray luminosity and is more consistent with the values inferred from PAH-dust 8 μm and the radio emission.

Furthermore, without the hot dust contribution from the torus, the PAH mass fraction is reduced by a factor of $\sim$3 in order to match the observed PAH EWs. In the non-torus models, therefore, $q_{\rm PAH}$ is a factor of $\sim$9 smaller for the IRAS16399N nucleus than the IRAS16399S nucleus. This is difficult to reconcile with the observed PAH fluxes, which are larger for the IRAS16399N nucleus, as indicated by the fluxes derived from the IRS spectra (Tables 1 and 4).

The parameters recovered for the torus component suggest that the AGN is embedded in a quasi-spherical (angular scale height $\gtrsim 66^\circ$), radially extended (outer radius $\gtrsim 60\times$ the dust sublimation radius) distribution of highly optically thick clumps ($\tau_V \approx A_V \sim 27$), with the average number of clumps along a given ray varying from $\gtrsim$14 at the equator to $\sim$3 along the poles ($\sim$14 clouds would intercept the line of sight at $i \sim 60^\circ$. The torus itself is screened by another $\approx$9 mag of visual extinction. Therefore, the AGN is deeply embedded in an effectively complete cocoon of dusty clumps, each of which is individually highly opaque. This is consistent with the detection of water ice and HAC absorption bands in the IRAS16399N nucleus; it seems likely that these features originate in the torus clumps.

This quasi-spherical "cocoon" of dusty gas would also be highly Compton-thick and this seems consistent with the weakness of the X-ray source associated with IRAS16399N, relative to the inferred bolometric luminosity of the AGN. Given a bolometric correction factor $\sim$20 (Elvis et al. 2004; Lusso et al. 2012), we predict an intrinsic 0.5–2 keV luminosity of $L_{0.5-2\,\rm keV} \approx 1.7 \times 10^{43}$ erg s^{-1} for the embedded AGN, compared with an observed luminosity of $\approx 5 \times 10^{40}$ erg s^{-1}.

5.4. Is the OH Maser Emission Associated with the AGN?

The location of the OHM source(s) in IRAS16399−0937 is, unfortunately, unknown, since there are no extant high resolution interferometry data at the OH line frequencies. However, Willett et al. (2011a, 2011b) find that, in comparison with a control sample of non-OHMG ULIRGs, the OHMGs preferentially exhibit H_2O and HAC bands and (as observed in the IRAS16399N nucleus) steeper mid-IR spectra. Therefore, it seems reasonable to conclude that the OH masers also reside in the IRAS16399N nucleus, presumably in the torus clumps. Indeed, the currently favored model for OHM emission invokes a clumpy medium, with individual clumps generating low-gain unsaturated emission while strong compact sources occur when the line of sight intersects multiple clouds (Parra et al. 2005). The pumping calculations of Lockett & Elitzur (2008) indicate that the masers are strongly radiatively pumped at 53 μm, with line overlap effects caused by internal cloud turbulence $\sim$20 km s^{-1} also playing an important role. In their model maximum maser inversion occurs for dust optical depths $10 \lesssim \tau_V \lesssim 50$ and dust temperatures $80 \lesssim T_d \lesssim 140$ K. The structural and physical properties of the torus component of the SED model fitted to the IRAS16399N nucleus are a good match to these conditions: the torus emission peaks in the 40–50 μm range, a typical sight-line intercepts multiple clouds ($\sim$14), individual clouds have optical depths $\tau_V \approx 27$ and for distances $\gtrsim 10 r_{\rm in}$ (where $r_{\rm in}$ is taken to be the dust sublimation radius, Section 4.1), the dust temperature in the cloud interior is $\lesssim$140 K (Nenkova et al. 2008a). Thus, the IRAS16399N nucleus, and specifically the AGN-heated torus, appears to have all the necessary ingredients for strong, radiatively pumped OH masers. Nonetheless, high-resolution radio interferometry measurements are needed to locate unambiguously determine the location of the OH masers relative to the double nucleus.

5.5. The Origin of the LINER Spectrum

The overall covering factor of the torus is close to unity, implying that only a very small fraction ($\leqslant$0.2%) of the ionizing photons produced by the AGN escape to photoionize the surrounding gas. If this is correct, radiation from the AGN itself fails by a factor of $\gtrsim$66 to account for the Hα flux measured from the IRAS16399N nucleus, even if all the ionizing photons that escape are absorbed in photoionizing the surrounding gas. Alternatively, we would require at least 5% of the AGN ionizing photons to escape, implying a covering factor $C_{\rm tor} \approx 0.95$, which is ruled out by the posterior probability distribution for this parameter (Figure 14).

It follows that the LINER spectrum of the IRAS16399N nucleus cannot be due to photoionization by the AGN. However, optical emission line ratios characteristic of LINERs can also be produced by several other mechanisms, including shocks (Dopita & Sutherland 1995; Allen et al. 2008), hot evolved (post-asymptotic giant branch) stars (e.g., Binette et al. 1994), and, in dense environments, young massive stars (e.g., Barth & Shields 2000). Any of these alternative ionization mechanism could plausibly be operating at some level in the IRAS16399N nucleus of IRAS16399-0937, but, given that gravitational torques are expected to drive gas flows in merging systems, shock ionization seems the most likely candidate. Indeed, inspection of the shock model grids presented by Allen et al. (2008) reveals that models including a photoionized precursor match the [O III]/Hβ, [O I]/Hα, [N II]/Hα and [S II]/Hα line ratios reported by Baan et al. (1998) and Kewley et al. (2001) remarkably well for shock velocities $\approx$100–200 km s^{-1}. Such shock velocities are comparable with radial inflow velocities found in gas dynamical simulations (e.g., Iono et al. 2004). Similarly, Monreal-Ibero et al. (2006) found that extended emission line regions in several ULIRGs have LINER-like ionization conditions consistent with shock ionization, which they attribute to shocks associated with merger-driven gas flows. Curiously, therefore, the results of the SED fitting support the presence of an AGN in the IRAS16399N nucleus, but also suggest that the LINER spectrum, upon which the original classification was based, is not due to AGN photoionization. The case of IRAS16399N exemplifies the point that a LINER spectrum does not necessarily indicate

the presence of an AGN. As 22.5% and 42% of the OHMGs studied by, respectively, Baan et al. (1998) and Darling & Giovanelli (2006) were spectroscopically classified as LINERs, misinterpretation of these objects as AGNs may partly explain the discrepancy between the high AGN fraction inferred in OHMG from optical spectroscopy (∼70%) and the much lower estimates obtained from radio, mid-IR and X-ray studies (10%–30%; Willett et al. 2011a, 2011b; Vignali et al. 2005).

It is worth noting, however, that Yuan et al. (2010) have recently argued that most previous LINER identifications in (U)LIRGs should be reclassified as composite starburst/AGN systems, based on the refined optical classification scheme introduced by Kewley et al. (2006). They conclude that "true" LINERs (in the sense of low accretion rate AGNs) rarely occur in IR luminous mergers. The IRAS16399N nucleus of IRAS16399−0937 is one of only 9 objects that are classified as LINERs in their sample of ∼500 (U)LIRGs. Nevertheless, as it falls near the Seyfert-LINER boundary in the VO diagrams, Yuan et al. (2010) suggest that it may be a Seyfert, or an intermediate object.[22] Conversely, our results suggest that the LINER spectrum originates from shock ionization and therefore is not directly related to the deeply embedded AGN.

5.6. Nuclear Gas Flows

Taking the black hole masses ($M_{\rm BH} \approx 10^8\ M_\odot$) derived from the Marconi & Hunt (2003) relation at face value, the inferred AGN luminosity ($L_{\rm bol} \approx 3.4 \times 10^{44}$ erg s^{-1}) implies a small Eddington ratio $L_{\rm bol}/L_{\rm Edd} \sim 10^{-2}$; where $L_{\rm Edd} \sim 10^{46}$ erg s^{-1} is the Eddington luminosity. The black hole in the IRAS16399N nucleus is therefore accreting at well below the Eddington rate, while, as there is no evidence for an AGN in the IRAS16399S nucleus, its black hole is presumably accreting at an even lower rate. Similarly, the SFRs in both nuclei are relatively modest (∼ 3–12 $M_\odot$ yr^{-1}) and the bulk of the current star formation ($\gtrsim$60%) is occurring in extended regions throughout the IRAS16399−0937 system. Evidently the merger, while triggering widespread star formation has not (yet) resulted in the massive gas inflows that would lead to vigorous nuclear starbursts and enhanced BH accretion.

In the case of IRAS16399−0937, therefore, the OHM emission does not appear to be associated with a transient enhancement in tidally driven gas inflows, as proposed by Darling (2007).

6. SUMMARY AND CONCLUSIONS

We have presented a multi-wavelength study of the LIRG IRAS16399−0937. This system is a gas-rich, mid-stage merger containing an OHM and consisting of two nuclei separated by ∼3.4 kpc, situated in a common envelope. In previous works, the nuclei have been classified on the basis of optical emission line ratios as a LINER (IRAS16399N) and a starburst (IRAS16399S), respectively. The data set analyzed here combines new emission line (Hα+[N II]) and broad-band (FR914M, F814W) imaging obtained with the *HST* ACS Wide Field Camera with archival imaging and spectroscopy in the optical (*HST* ACS F435W), near infrared (*HST* NICMOS 1.6 μm, 2MASS *J* and *K*), mid/far-infrared (*Spitzer* IRAC, IRS and MIPS), submillimeter (*Herschel* SPIRE), and radio (1.49 and 4.9 GHz VLA). The main results from this analysis are summarized below.

1. The *HST* images reveal a complex system of dust lanes and emission line knots and filaments. Aside from the two nuclei, the main morphological features are a large (∼3 kpc) diffuse region of star formation extending north and east of the IRAS16399N nucleus and an arc-like structure, also including star formation regions (as traced by Hα+[N II] line emission and *B*-band continuum) curving around the Western side of the system, which connects the IRAS16399S nucleus to the NE diffuse region. An extensive dust lane complex running E–W separates the nuclei while the IRAS16399N nucleus itself is crossed by a dust lane oriented SE–NE.
2. PAH emission at 8 μm occupies the interior of envelope, with bright peaks corresponding to the two nuclei and spurs associated with the NE diffuse region and the dust lane complex E of the nuclei. The extended radio source morphology is very similar to that of the PAH emission, suggesting that it is due to star formation. Similarly, we find that the radio core associated with the IRAS16399N nucleus has a spectral index ($\alpha = -0.75 \pm 0.08$) and brightness temperature ($\sim 2.3 \times 10^4$ K) consistent with star formation rather than an AGN jet, in agreement with Baan & Klöckner's (2006) earlier classification.
3. Star formation activity is widespread throughout the system but mostly heavily obscured. The SFR for the system as a whole as derived from radio and IR luminosities is $\sim 20 M_\odot$ yr^{-1}, a factor of ∼4 greater than the rate obtained from the Hα emission. The two nuclei together account for only ≈30%–60% of the total. Although the two nuclei have similar stellar masses (as indicated by their *H*-band luminosities), the IRAS16399N nucleus is brighter in both PAH and radio, indicating a higher SFR.
4. The *Spitzer* IRS spectrum (5.2–37 μm) of the whole system is characterized by deep silicate absorption, PAH emission features, vibrational lines of H_2, and ionic lines from species of moderate IP (IP < 50 eV) such as [Ar II], [Ne III] and [S III]. Absorption bands of water ice (6.0 μm) and hydrogenated amorphous carbon (6.85 and 7.25 μm) are also present. The higher spatial resolution in SL mode also allows separate extractions in the wavelength range 5.2–14 μm for the two nuclei and for several locations along the slit sampling the ISM of the extended envelope. The two nuclei show similar spectral features but the IRAS16399N nucleus exhibits the deepest ice and HAC absorption bands and is distinguished by a steeply rising continuum at wavelengths > 12 μm. The H_2O and HAC bands indicate the presence of compact and cold material, while the steep continuum is likely due to warm dust from an AGN-heated torus. However, we do not detect the high ionization fine structure lines (e.g., [Ne V] 14.3 μm), which are widely regarded as tracers of AGN activity, in either nucleus. In general, the ISM mid-IR spectra in the 5.2–14 μm band show prominent PAH features, but the H_2O and HAC absorption bands and ionic emission lines are weaker or absent.
5. Decomposition of the optical—FIR SED of the two nuclei of IRAS16399−0937 into stellar, dusty ISM, and AGN torus components confirms the presence of a moderately luminous AGN ($L_{\rm bol} \approx 3.4 \times 10^{44}$ erg s^{-1}) in the IRAS16399N nucleus. However, the torus parameters recovered from the fit indicate that the AGN is completely embedded in a quasi-spherical distribution of optically thick

[22] The distribution of the Sloan Digital Sky Survey data in these diagrams shows that Seyferts and LINERs occupy distinct branches.

clumps. This structure has a covering factor close to unity, implying that only a very small fraction ($\leqslant$0.2%) of the photons produced by the AGN escape. The SED fits are consistent with SFRs of $\sim$12 and 3 $M_\odot$ yr^{-1} for the IRAS16399N and IRAS16399S nucleus, respectively. These values are consistent with that inferred from the X-ray emission and are (within a factor of $\sim$2–3) of the SFRs derived from the ISM PAH-dust 8 μm emission and the radio emission. However, if the AGN torus is omitted from the SED model, the SFR inferred for IRAS16399N increases to $\sim$20 $M_\odot$ yr^{-1}, which is comparable with the value determined for the entire system. The properties of the clumpy "torus" are consistent with the conditions required for strong, radiatively pumped OH maser emission.

6. The small fraction of ionizing photons that escapes the torus is insufficient to produce the observed Hα luminosity from the IRAS16399N nucleus by a factor of $\sim$66. It follows that the LINER emission line spectrum cannot be attributed to AGN photoionization. We propose instead that the line emission from the IRAS16399N nucleus is due to shocks with velocities $\approx$100–200 km s^{-1}, perhaps associated with gas flows induced by gravitational torques generated by the merger.
7. If the IRAS16399N nucleus follows the Marconi & Hunt scaling relationship between *H*-band luminosity and black hole mass, the luminosity derived for the embedded AGN implies that the $\sim 10^8$ $M_\odot$ black hole is accreting at a small fraction ($\sim$1%) of the Eddington rate. As the SFRs in both nuclei are also relatively modest, it seems clear that the massive gas inflows predicted by merger simulations have yet to fully develop in this system.

The picture that emerges of IRAS16399−0937 is that of a gas-rich merger of mass ratio $\approx$1:1. The merger has triggered widespread star formation but massive gas flows into the still distinct nuclei have not yet fully developed. The IRAS16399N nucleus harbors an embedded AGN of relatively modest luminosity and is also the likely source of the OHM emission, while the IRAS16399S nucleus is starburst dominated. The AGN is apparent almost entirely through the contribution of AGN-heated dust to the IR SED. The LINER optical spectrum upon which the original classification was based is probably due to shocks, rather than AGN photoionization. This work also highlights the value of multiwavelength data and spatial resolution in establishing the nature of the buried power sources in (U)LIRGs.

We thank the anonymous referee for useful comments that improved the clarity of the paper. Support for program 11604 was provided by NASA through a grant from the Space Telescope Science Institute, which is operated by the Association of Universities for Research in Astronomy, Inc., under NASA contract NAS 5-26555. This material is based upon work partly supported by the National Aeronautics and Space Administration under grant No. NNX11AI03G issued through the Science Mission Directorate. D. A. Sales gratefully acknowledge for partial financial support received from FAPERGS/CAPES n.05/2013.

APPENDIX

FITTING THE SED WITH CLUMPYDREAM

The stellar, ISM, and AGN torus components of the SED were computed on parameter grids; the parameters and their grid values are exhaustively listed in Table 6. The number of possible model combinations is 2.4×10^9. One search strategy would be to sample all of the grid points exhaustively. At each grid point, the corresponding stellar, ISM, and AGN torus components are generated, and their normalizations are determined by a fit to the observed SED. The best fits, determined by minimum χ^2 or maximum-likelihood, out of all of the grid points would then represent the best decomposition. Although the model is a linear combination of SED components, the requirement of non-negative coefficients, the use of censored data (upper limits from large apertures), and the inclusion of foreground extinction require non-linear fitting methods at any set of grid points. At this time, performing non-linear fits over 10^9 parameter combinations is computationally prohibitive.

clumpyDREAM instead performs a Markov Chain Monte Carlo (MCMC) search over the parameter grid. This approach has become commonplace for SED fitting (e.g., recently, Pirzkal et al. 2012; Serra et al. 2011; Asensio Ramos & Ramos Almeida 2009; Ptak et al. 2007; Sajina et al. 2006) because of its economy and efficiency over an exhaustive search over large parameter spaces. The commonest approach is to use the random walk Metropolis (RWM) algorithm (Metropolis et al. 1953; Hastings 1970). However, RWM inefficiently samples complex or multimodal probability distributions, especially when modes are widely separated (see Abraham & Haines 1999). We found widely spaced modes to be a problem especially for SEDs showing silicate in emission. This inefficiency is somewhat mitigated by adaptively tuning the step-size in parameter space (Haario et al. 1999, 2001), but our experience is that the tuning can be adversely affected by parameter boundaries, causing solutions to hang up on local χ^2 minima. Furthermore, single-chain adaptive RWM still has difficulty with widely spaced modes.

The DREAMZS algorithm (ter Braak & Vrugt 2008) involves a more robust, self-adapting stepper with multiple chains, and we employed a modified version of DREAMZS in clumpyDREAM. The DREAMZS algorithm uses differential evolution (DE; Storn & Price 1997) to determine steps in parameter space. Multiple parameter chains are run in parallel, with the current state of all chains stored in $\mathbf{X}$, where $\mathbf{X}_i$ is the *i*th vector out of an evolving population of parameter vectors. The history of accepted parameter vectors is stored in $\mathbf{Z}$, where $\mathbf{Z}_j$ is the parameter vector of the *j*th member of the chain. Trial solutions $\widetilde{\mathbf{X}}$ are generated by,

$$\widetilde{\mathbf{X}}_i = \mathbf{X}_i + \gamma(1 + \mathbf{e})\,(\mathbf{Z}_m - \mathbf{Z}_n) + \epsilon, \qquad \text{(A1)}$$

where $\mathbf{Z}_m$ and $\mathbf{Z}_n$ are randomly drawn, without replacement, from the history of solutions, $\mathbf{e}$ contains uniform random deviates in the range -0.05 to 0.05, and ϵ is a vector of normal random deviates with standard deviation 10^{-6}. The spirit of the DE stepper is to use the sampling history as a measure of the covariance matrix, and the term γ sets the scale of the step size relative to the spread of parameter values. Following the recommendations of ter Braak & Vrugt, $\gamma = 2.38/\sqrt{2p}$, where p is the number of parameters being adjusted at a given step. The tuning schedule is adapted from that used by Patil et al. (2010) for their implementation of the adaptive RWM algorithm. Otherwise, new solutions are accepted or rejected using the usual Metropolis (likelihood) ratio criterion. The algorithm therefore returns samples from the posterior probability distribution of the model parameters subject to prior assumptions or constraints. Here, the main prior constraints are imposed by the domain of the gridded parameters.

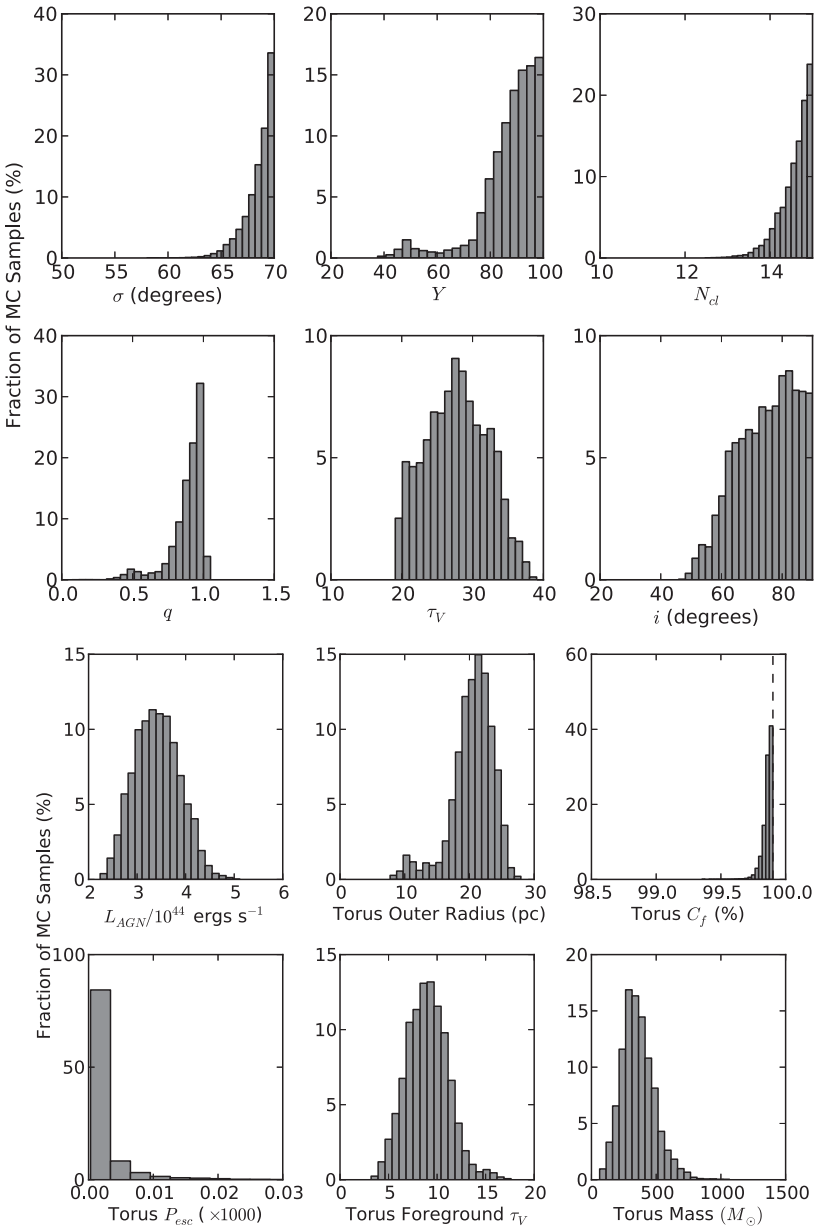

Figure 14. Marginalized posterior probability densities estimated from the MCMC samples for the parameters derived from the clumpyDREAM SED fits to IRAS16399−0937. Torus parameters for the IRAS16399N nucleus in the AGN+starburst model.

clumpyDREAM also employs the snooker updater, a modification of the DE stepper, every 10 iterations, as described by ter Braak & Vrugt (2008). Since both the DE and snooker methods operate on continuous parameters, it was necessary to interpolate the gridded models. We used multidimensional linear splines, which provided stable solutions. In contrast, cubic spline interpolation introduced artifacts such as ringing and negative values in the interpolated SEDs, which indicates that over some regions of parameter space the model grids sample changes in the shape of the SED insufficiently for the use of higher-order interpolation methods.

For each Monte Carlo trial, the clumpyDREAM procedure ordinarily involves two steps: (1) selection of model parameters by either DE or the snooker updater, and (2) determining the linear coefficients for each model component by a linear, least-squares fit. The data for IRASF16399−0937 present a challenge, however, that the SEDs for each of the two nuclei are fit simultaneously subject to the constraint that the sum of the SEDs must fall under the upper limits imposed by large aperture data: i.e., far-infrared measurements, which do not resolve the two nuclei and include diffuse emission outside the extraction apertures used at shorter wavelengths. We therefore had to modify clumpyDREAM to treat the coefficients as non-linear parameters that are sampled by MCMC rather than determined by linear fits. Upper limits are then handled in a method similar to the In-Out technique (Friedman & Stuetzle 1981) if the sum of the model SEDs exceeds an upper limit, that upper limit is included in the calculation of the likelihood; otherwise, it is ignored.

clumpyDREAM randomly initializes $\mathbf{Z}$ with ∼100 randomly sampled parameter vectors. Initial parameters are drawn assuming uniform prior distributions before engaging the modified DREAMZS stepper. For the gridded models, parameters were randomly selected within their range of support (Table 6). Values for the foreground extinction were randomly selected from values ranging from $\tau_V = 0$ to 100, but any $\tau_V > 0$ was permitted during MCMC sampling.

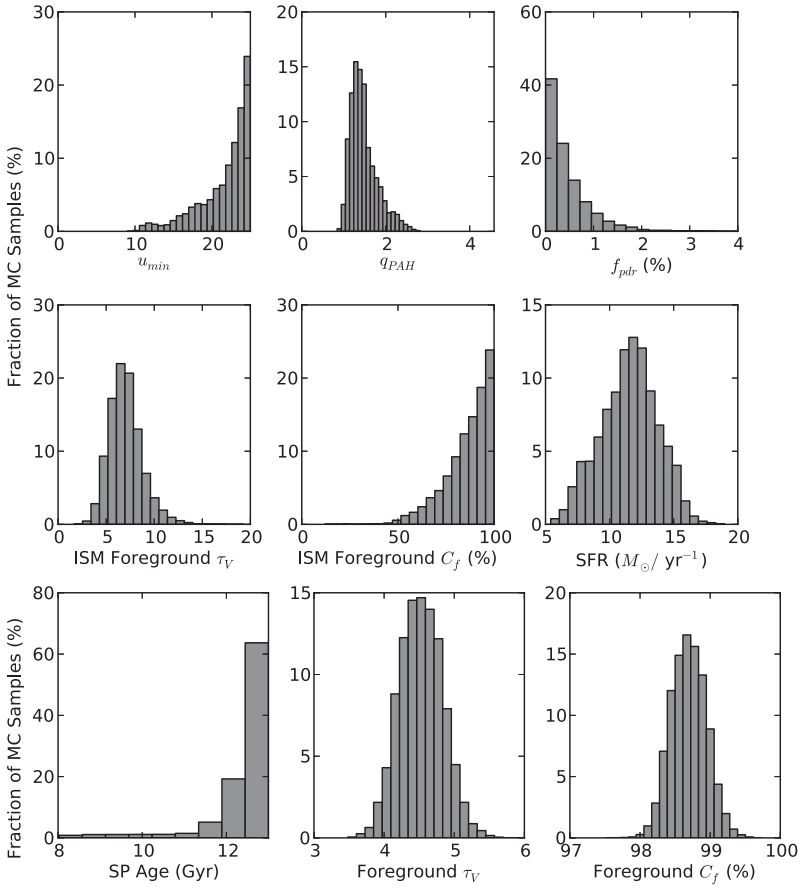

Figure 15. Same as Figure 14, for the parameters of the stellar and ISM components.

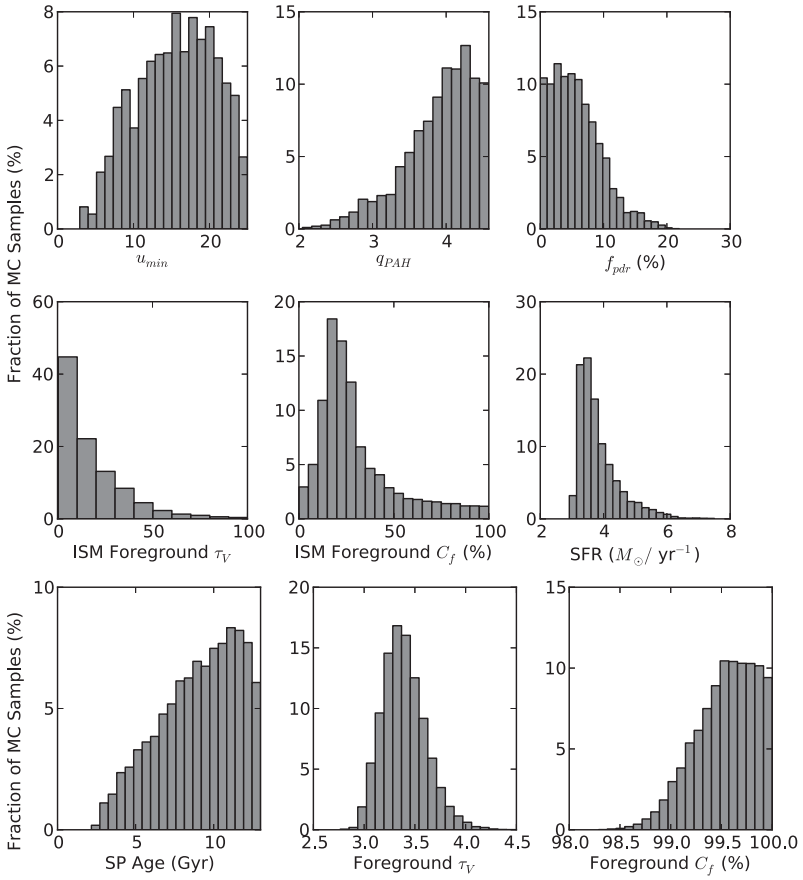

Figure 16. Same as Figure 15 for the IRAS16399S nucleus.

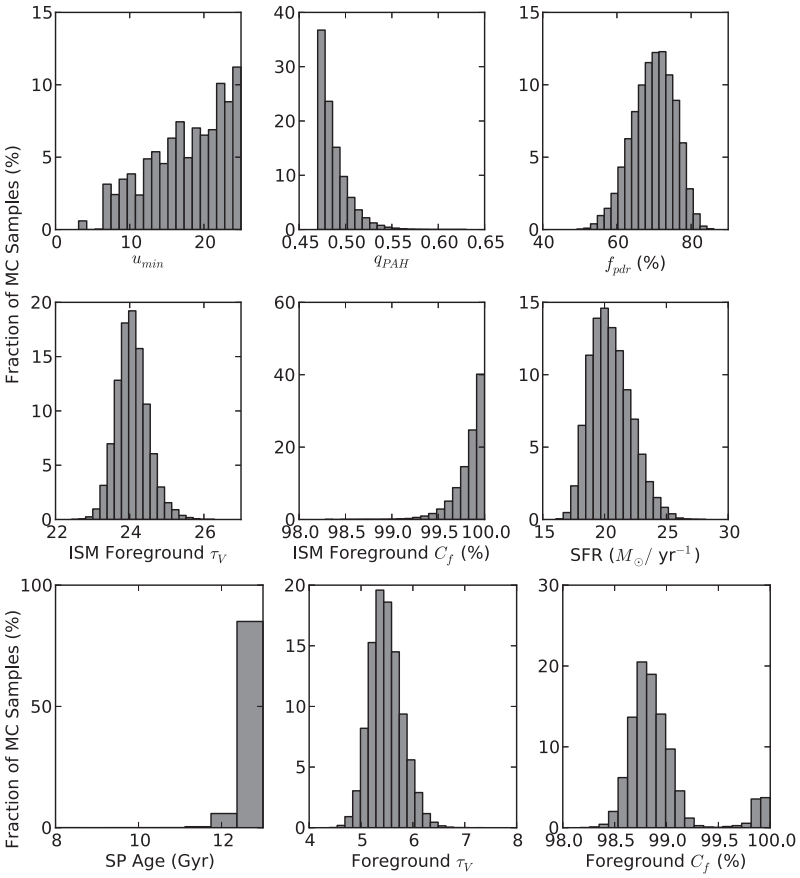

Figure 17. Probability density distributions of the parameters derived from the clumpyDREAM SED fits to IRAS16399−0937. Parameters of the stellar and ISM components for the IRAS16399N nucleus in the starburst+starburst model.

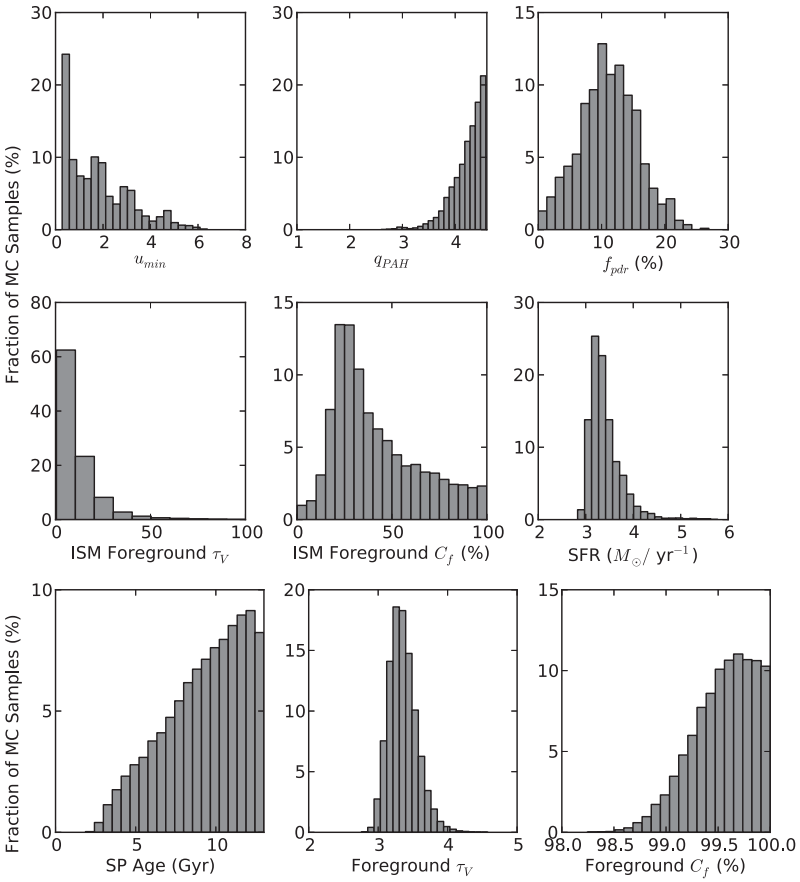

Figure 18. Same as Figure 17 for the IRAS16399S nucleus.

Foreground covering fractions were sampled from and restricted to $C_f = 0$–1.

Multiple, parallel chains are necessary for the DE algorithm, but they also provide a means of sampling multimodal distributions more efficiently than RWM or its variants. To test this assertion, the modified version of clumpyDREAM was initially applied to the observed SED of IRASF16399−0937 in 20 short-run trials to search for possibly widely separated modes. In each run, five chains were run in parallel, and solutions were thinned by concatenating the parameter vector population $\widetilde{\mathbf{X}}$ onto the chains $\widetilde{\mathbf{Z}}$ every tenth iteration. All of the short-run trials converged to indistinguishable posterior distributions despite starting from different, randomly generated parent chains. Based on the success of these trial runs, clumpyDREAM was reinitialized and allowed to run a minimum of 10^5 iterations and until the distribution of likelihood values reached a stationary state as measured by the Geweke statistic (Geweke 1992).

REFERENCES

Abraham, K. J., & Haines, L. M. 1999, JCoPh, 155, 380
Allamandola, L. J., Tielens, A. G. G. M., & Barker, J. R. 1985, ApJL, 290, L25
Allen, M. G., Groves, B. A., Dopita, M. A., Sutherland, R. S., & Kewley, L. J. 2008, ApJS, 178, 20
Antonucci, R. 1993, ARA&A, 31, 473
Antonucci, R. R. J., & Miller, J. S. 1985, ApJ, 297, 621
Armus, L., Charmandaris, V., Bernard-Salas, J., et al. 2007, ApJ, 656, 148
Armus, L., Mazzarella, J. M., Evans, A. S., et al. 2009, PASP, 121, 559
Asensio Ramos, A., & Ramos Almeida, C. 2009, ApJ, 696, 2075
Baan, W. A. 1985, Natur, 315, 26
Baan, W. A., & Klöckner, H.-R. 2006, A&A, 449, 559
Baan, W. A., Salzer, J. J., & Lewinter, R. D. 1998, ApJ, 509, 633
Baldwin, J. A., Phillips, M. M., & Terlevich, R. 1981, PASP, 93, 5
Barnes, J. E., & Hernquist, L. 1992, ARA&A, 30, 705
Barth, A. J., & Shields, J. C. 2000, PASP, 112, 753
Baum, S. A., Gallimore, J. F., O'Dea, C. P., et al. 2010, ApJ, 710, 289
Bendo, G. J., Buckalew, B. A., Dale, D. A., et al. 2006a, ApJ, 645, 134
Bendo, G. J., Dale, D. A., Draine, B. T., et al. 2006b, ApJ, 652, 283
Binette, L., Magris, C. G., Stasińska, G., & Bruzual, A. G. 1994, A&A, 292, 13
Bohlin, R. C., Savage, B. D., & Drake, J. F. 1978, ApJ, 224, 132
Brandl, B. R., Bernard-Salas, J., Spoon, H. W. W., et al. 2006, ApJ, 653, 1129
Calzetti, D., Kennicutt, R. C., Jr., Bianchi, L., et al. 2005, ApJ, 633, 871
Calzetti, D., Kennicutt, R. C., Engelbracht, C. W., et al. 2007, ApJ, 666, 870
Chiar, J. E., Tielens, A. G. G. M., Whittet, D. C. B., et al. 2000, ApJ, 537, 749
Clemens, M. S., Vega, O., Bressan, A., et al. 2008, A&A, 477, 95
Condon, J. J. 1983, ApJS, 53, 459
Condon, J. J., Cotton, W. D., & Broderick, J. J. 2002, AJ, 124, 675
Condon, J. J., Huang, Z.-P., Yin, Q. F., & Thuan, T. X. 1991, ApJ, 378, 65
Darling, J. 2007, ApJL, 669, L9
Darling, J., & Giovanelli, R. 2002, ApJ, 572, 810
Darling, J., & Giovanelli, R. 2006, AJ, 132, 2596
Dartois, E., Geballe, T. R., Pino, T., et al. 2007, A&A, 463, 635
Diamond-Stanic, A. M., & Rieke, G. H. 2010, ApJ, 724, 140
Dopita, M. A., & Sutherland, R. S. 1995, ApJ, 455, 468
Draine, B. T. 2003, ARA&A, 41, 241
Draine, B. T., Dale, D. A., Bendo, G., et al. 2007, ApJ, 663, 866
Draine, B. T., & Li, A. 2001, ApJ, 551, 807
Draine, B. T., & Li, A. 2007, ApJ, 657, 810
Elitzur, M., & Shlosman, I. 2006, ApJL, 648, L101
Elvis, M., Risaliti, G., Nicastro, F., et al. 2004, ApJL, 615, L25
Fazio, G. G., Hora, J. L., Allen, L. E., et al. 2004, ApJS, 154, 10
Fischera, J., & Dopita, M. 2005, ApJ, 619, 340
Fisher, D. B., & Drory, N. 2008, AJ, 136, 773
Friedman, J. H., & Stuetzle, W. 1981, Light Scattering by Small Particles, Technical Report No. 65, Division of Biostatistics, Stanford Univ.
Galliano, F., Madden, S. C., Tielens, A. G. G. M., Peeters, E., & Jones, A. P. 2008, ApJ, 679, 310
Gallimore, J. F., Yzaguirre, A., Jakoboski, J., et al. 2010, ApJS, 187, 172
Genzel, R., & Cesarsky, C. J. 2000, ARA&A, 38, 761
Genzel, R., Lutz, D., Sturm, E., et al. 1998, ApJ, 498, 579
Georgantopoulos, I., & Akylas, A. 2010, A&A, 509, A38
Geweke, J. 1992, in Bayesian Statistics, ed. J. M. Bernardo, J. O. Berger, A. P. Dawid, & A. F. Smith (Oxford: Clarendon Press), 169
Gioia, I. M., Gregorini, L., & Klein, U. 1982, A&A, 116, 164
Giroletti, M., & Panessa, F. 2009, ApJL, 706, L260
Griffin, M. J., Abergel, A., Abreu, A., et al. 2010, A&A, 518, L3
Haan, S., Surace, J. A., Armus, L., et al. 2011, AJ, 141, 100
Haario, H., Saksman, E., & Tamminen, J. 1999, Comput. Stat., 14, 375
Haario, H., Saksman, E., & Tamminen, J. 2001, Bernoulli, 7, 223
Haas, M., Klaas, U., & Bianchi, S. 2002, A&A, 385, L23
Hastings, W. 1970, Biometrika, 57, 97
Heckman, T. M. 1980, A&A, 87, 152
Helou, G., Lu, N. Y., Werner, M. W., Malhotra, S., & Silbermann, N. 2000, ApJL, 532, L21
Helou, G., Roussel, H., Appleton, P., et al. 2004, ApJS, 154, 253
Higdon, S. J. U., Devost, D., Higdon, J. L., et al. 2004, PASP, 116, 975
Ho, L. C. 2008, ARA&A, 46, 475
Ho, L. C. 2009, ApJ, 699, 626
Hoopes, C. G., Walterbos, R. A. M., & Rand, R. J. 1999, ApJ, 522, 669
Hopkins, P. F., Hernquist, L., Cox, T. J., et al. 2006, ApJS, 163, 1
Houck, J. R., Roellig, T. L., van Cleve, J., et al. 2004, ApJS, 154, 18
Iono, D., Yun, M. S., & Mihos, J. C. 2004, ApJ, 616, 199
Jin, C., Ward, M., & Done, C. 2012, MNRAS, 422, 3268
Kewley, L. J., Groves, B., Kauffmann, G., & Heckman, T. 2006, MNRAS, 372, 961
Kewley, L. J., Heisler, C. A., Dopita, M. A., & Lumsden, S. 2001, ApJS, 132, 37
Kharb, P., Hota, A., Croston, J. H., et al. 2010, ApJ, 723, 580
Klöckner, H.-R., & Baan, W. A. 2004, A&A, 419, 887
Kormendy, J., Bender, R., & Cornell, M. E. 2011, Natur, 469, 374
Kormendy, J., & Kennicutt, R. C., Jr. 2004, ARA&A, 42, 603
Kukula, M. J., Ghosh, T., Pedlar, A., & Schilizzi, R. T. 1999, ApJ, 518, 117
Lahav, O., & Liddle, A. R. 2014, arXiv:1401.1389
Lebouteiller, V., Bernard-Salas, J., Sloan, G. C., & Barry, D. J. 2010, PASP, 122, 231
Leger, A., & Puget, J. L. 1984, A&A, 137, L5
Li, A., & Draine, B. T. 2001, ApJ, 554, 778
Li, A., & Draine, B. T. 2002, ApJ, 576, 762
Lo, K. Y. 2005, ARA&A, 43, 625
Lockett, P., & Elitzur, M. 2008, ApJ, 677, 985
Lusso, E., Comastri, A., Simmons, B. D., et al. 2012, MNRAS, 425, 623
Magdis, G. E., Daddi, E., Béthermin, M., et al. 2012, ApJ, 760, 6
Makovoz, D., & Khan, I. 2005, in ASP Conf. Ser. Vol. 347, Astronomical Data Analysis Software and Systems (ADASS) XIV, ed. P. Shopbell, M. Britton, & R. Ebert (San Francisco, CA: ASP), 81
Makovoz, D., Khan, I., & Moshir, M. 2005, PASP, 117, 274
Makovoz, D., & Marleau, F. R. 2005, PASP, 117, 1113
Marconi, A., & Hunt, L. K. 2003, ApJL, 589, L21
Mathis, J. S., Mezger, P. G., & Panagia, N. 1983, A&A, 128, 212
Metropolis, N., Rosenbluth, A. W., Rosenbluth, M. N., Teller, A. H., & Teller, E. 1953, J. Chem. Phys., 21, 1087
Micelotta, E. R., Jones, A. P., & Tielens, A. G. G. M. 2010a, A&A, 510, A37
Micelotta, E. R., Jones, A. P., & Tielens, A. G. G. M. 2010b, A&A, 510, A36
Momjian, E., Romney, J. D., Carilli, C. L., & Troland, T. H. 2006, ApJ, 653, 1172
Monreal-Ibero, A., Arribas, S., & Colina, L. 2006, ApJ, 637, 138
Mor, R., Netzer, H., & Elitzur, M. 2009, ApJ, 705, 298
Nenkova, M., Sirocky, M. M., Ivezić, Ž., & Elitzur, M. 2008a, ApJ, 685, 147
Nenkova, M., Sirocky, M. M., Nikutta, R., Ivezić, Ž., & Elitzur, M. 2008b, ApJ, 685, 160
Norris, R. P., Gardner, F. F., Whiteoak, J. B., Allen, D. A., & Roche, P. F. 1989, MNRAS, 237, 673
O'Dowd, M. J., Schiminovich, D., Johnson, B. D., et al. 2009, ApJ, 705, 885
Ott, S. 2010, in ASP Conf. Ser. 434, Astronomical Data Analysis Software and Systems XIX, ed. Y. Mizumoto, K.-I. Morita, & M. Ohishi (San Francisco, CA: ASP), 139
Parra, R., Conway, J. E., Elitzur, M., & Pihlström, Y. M. 2005, A&A, 443, 383
Patil, A., Huard, D., & Fonnesbeck, C. J. 2010, J. Stat. Software, 35, 1
Peeters, E., Martín-Hernández, N. L., Damour, F., et al. 2002, A&A, 381, 571
Peeters, E., Spoon, H. W. W., & Tielens, A. G. G. M. 2004, ApJ, 613, 986
Petric, A. O., Armus, L., Howell, J., et al. 2011, ApJ, 730, 28
Pihlström, Y. M., Baan, W. A., Darling, J., & Klöckner, H.-R. 2005, ApJ, 618, 705
Pirzkal, N., Rothberg, B., Nilsson, K. K., et al. 2012, ApJ, 748, 122
Planck Collaboration, Ade, P. A. R., Aghanim, N., et al. 2013, arXiv:1303.5076
Ptak, A., Mobasher, B., Hornschemeier, A., Bauer, F., & Norman, C. 2007, ApJ, 667, 826
Puget, J. L., & Leger, A. 1989, ARA&A, 27, 161
Ranalli, P., Comastri, A., & Setti, G. 2003, A&A, 399, 39

Reach, W. T., Megeath, S. T., Cohen, M., et al. 2005, PASP, 117, 978
Richards, A. M. S., Knapen, J. H., Yates, J. A., et al. 2005, MNRAS, 364, 353
Rieke, G. H., Alonso-Herrero, A., Weiner, B. J., et al. 2009, ApJ, 692, 556
Rieke, G. H., Young, E. T., Engelbracht, C. W., et al. 2004, ApJS, 154, 25
Rigopoulou, D., Spoon, H. W. W., Genzel, R., et al. 1999, AJ, 118, 2625
Rossa, J., & Dettmar, R.-J. 2000, A&A, 359, 433
Rossa, J., & Dettmar, R.-J. 2003, A&A, 406, 505
Rovilos, E., Diamond, P. J., Lonsdale, C. J., & Smith, H. E. 2002, in Proc. the 6th EVN Symposium, ed. E. Ros, R. W. Porcas, A. P. Lobanov, & J. A. Zensus, 179
Roy, A. L., Ulvestad, J. S., Wilson, A. S., et al. 2000, in Perspectives on Radio Astronomy: Science with Large Antenna Arrays, ed. M. P. van Haarlem, 173
Rupke, D. S. N., Veilleux, S., & Baker, A. J. 2008, ApJ, 674, 172
Sadler, E. M., Slee, O. B., Reynolds, J. E., & Roy, A. L. 1995, MNRAS, 276, 1373
Sajina, A., Scott, D., Dennefeld, M., et al. 2006, MNRAS, 369, 939
Sales, D. A., Pastoriza, M. G., & Riffel, R. 2010, ApJ, 725, 605
Sanders, D. B., & Mirabel, I. F. 1996, ARA&A, 34, 749
Sanders, D. B., Soifer, B. T., Elias, J. H., et al. 1988a, ApJ, 325, 74
Sanders, D. B., Soifer, B. T., Elias, J. H., Neugebauer, G., & Matthews, K. 1988b, ApJL, 328, L35
Schwartz, G. 1978, AnSta, 6, 461
Serra, P., Amblard, A., Temi, P., et al. 2011, ApJ, 740, 22
Silva, L., Granato, G. L., Bressan, A., & Danese, L. 1998, ApJ, 509, 103
Smith, J. D. T., Draine, B. T., Dale, D. A., et al. 2007, ApJ, 656, 770
Soifer, B. T., Sanders, D. B., Madore, B. F., et al. 1987, ApJ, 320, 238
Spoon, H. W. W., Keane, J. V., Tielens, A. G. G. M., et al. 2002, A&A, 385, 1022
Spoon, H. W. W., Keane, J. V., Tielens, A. G. G. M., Lutz, D., & Moorwood, A. F. M. 2001, A&A, 365, L353
Spoon, H. W. W., Marshall, J. A., Houck, J. R., et al. 2007, ApJL, 654, L49
Staveley-Smith, L., Norris, R. P., Chapman, J. M., et al. 1992, MNRAS, 258, 725
Staveley-Smith, L., Unger, S. W., Cohen, R. J., Chapman, J. M., & Pointon, L. 1986, IAU Circ., 4248, 2
Storn, R., & Price, K. 1997, J. Global Optimization, 11, 341
Sturm, E., Lutz, D., Tran, D., et al. 2000, A&A, 358, 481
Sturm, E., Lutz, D., Verma, A., et al. 2002, A&A, 393, 821
ter Braak, C., & Vrugt, J. 2008, Stat. Comput., 18, 435
Tielens, A. G. G. M. 2008, ARA&A, 46, 289
Treister, E., Schawinski, K., Urry, C. M., & Simmons, B. D. 2012, ApJL, 758, L39
Ulvestad, J. S., Antonucci, R. R. J., & Barvainis, R. 2005, ApJ, 621, 123
Urry, C. M., & Padovani, P. 1995, PASP, 107, 803
van Dokkum, P. G. 2001, PASP, 113, 1420
Veilleux, S., Kim, D.-C., & Sanders, D. B. 1999, ApJ, 522, 113
Veilleux, S., & Osterbrock, D. E. 1987, ApJS, 63, 295
Veilleux, S., Rupke, D. S. N., Kim, D.-C., et al. 2009, ApJS, 182, 628
Vignali, C., Brandt, W. N., Comastri, A., & Darling, J. 2005, MNRAS, 364, 99
Walcher, J., Groves, B., Budavári, T., & Dale, D. 2011, Ap&SS, 331, 1
Weingartner, J. C., & Draine, B. T. 2001, ApJ, 548, 296
Willett, K. W., Darling, J., Spoon, H. W. W., Charmandaris, V., & Armus, L. 2011a, ApJS, 193, 18
Willett, K. W., Darling, J., Spoon, H. W. W., Charmandaris, V., & Armus, L. 2011b, ApJ, 730, 56
Willmer, C. N. A., Rieke, G. H., Le Floc'h, E., et al. 2009, AJ, 138, 146
Wu, H., Cao, C., Hao, C.-N., et al. 2005, ApJL, 632, L79
Yates, J. A., Richards, A. M. S., Wright, M. M., et al. 2000, MNRAS, 317, 28
Yuan, T.-T., Kewley, L. J., & Sanders, D. B. 2010, ApJ, 709, 884
Yun, M. S., Reddy, N. A., & Condon, J. J. 2001, ApJ, 554, 803